[UCI]I804:21028-200000105270

공학석사 학위논문

스트레인게이지 및 광섬유 센서를 이용한 아라온호의 빙하중 계측데이터 비교 분석

-2015년 및 2016년 북극해 탐사자료-

Comparative Analysis of Ice Load Data using Strain Gauge Sensor and Fiber Optic Sensor on the IBRV ARAON in the Arctic Sea

-2015 and 2016 Arctic Voyage Data-

지도교수 최 경 식

2018년 8월

한국해양대학교 해양과학기술전문대학원

해양과학기술융합학과

전 민 철

본 논문을 전민철의 공학석사 학위논문으로 인준함.

위원장 : 공학박사 서 영 교 (인)

위 원 : 공학박사 박 선 호 (인)

위 원 : 공학박사 최 경 식 (인)

2018년 8월

한국해양대학교 해양과학기술전문대학원

해양과학기술융합학과

전 민 철

Table of Contents

List of Figures

List of Tables

Comparative Analysis of Ice Load Data using Strain Gauge Sensor and Fiber Optic Sensor on the IBRV ARAON in the Arctic Sea

-2015 and 2016 Arctic Voyage Data-

by

Mincheul Jeon

Department of Convergency Study on the Ocean Science and Technology,
Korea Maritime and Ocean University

Abstract

The estimation of ice loads acting on a ship hull is one of the most critical concerns from a design point of view. To estimate the ice loads, various types of related research have been conducted, including full-scale measurement tests, model tests, and numerical model tests.

To estimate the ice loads, ice load data recorded from a full-scale measurement test is necessary. The IBRV ARAON was used to conduct ice field tests in this study. To measure ice load data in ice field tests, strain gauges were installed on the inner hull plates and at the transverse frames of

ARAON's bow section. The measured strain data was analyzed to calculate ice loads using two approaches; i.e., the influence coefficient method and the calculation of shear force.

This study focuses on estimating the local ice load, which is calculated by shear strains at transverse frames and comparing to local ice load calculated by the influence coefficient matrix. The level of local ice loads estimated from shear strain measurement was a little lower than those of hull plates. As a result, the method using shear strain data is recommended concerning the cost and simple procedures. Additionally, this study is intended to verify the performance and the potential of fiber optic sensors. For the verification of the results, the peak ice loads and stresses calculated from fiber optic sensors were analysed and it was a little higher than those from strain gauge sensors. The fiber optic sensor is considered more suitable for measuring ice load data in harsh environments.

The presented results should be useful for future studies of local ice load estimation at the design part of a vessel. Also the analyzed results of strain data measured from fiber optic sensors can be helpful for the next ice field test.

KEY WORDS: Ice Field Test; Icebreaking Research Vessel ARAON;
Fiber Optic Sensor; Electrical Strain Gauge; Local Ice Load;

Chapter 1 Introduction

1.1 Background and Objectives

In recent years, the interest of natural resources buried in the Arctic Ocean has been increasing than in past decades, and the NASA announced that average Arctic sea ice extent set a record low, reflecting high air temperatures, wind, and a warm ocean. Figure 1-1 shows the average monthly Arctic sea ice extent each September since 1979, derived from satellite observations(NASA, 2017). September Arctic sea ice is declining at a rate of 13.2 percent per decade, relative to the 1981 to 2010 average. This phenomenon is expected to accelerate global warming quickly. With diminishing in Arctic sea ice extent by various factors, the use of the Northern Sea Route (NSR) that allows transit between Europe and Asia has been expanded for Arctic-going vessels. This tendency is expected to increase sharply the demand for ships such as shuttle tankers, bulk carriers, and research vessels that can be operated in ice-covered waters.

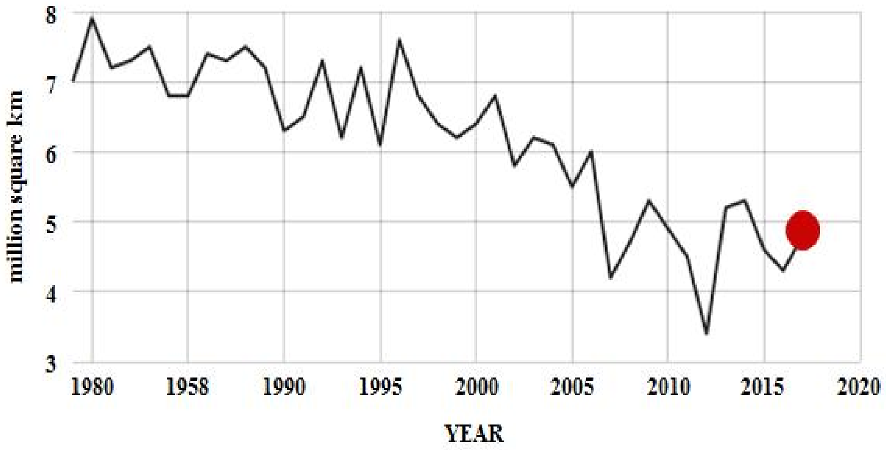

Fig. 1-1 Average monthly Arctic sea ice extent in September since 1979 (NASA, 2017)

Vessels in ice-covered waters are subjected to various harsh environmental loads such as wave loads, slamming forces. Meanwhile, the largest one that affected the vessel is the ice load. In particular, the estimation of ice load is related to hull form and propulsion power. However, estimating the ice loads is considerably complicated because of irregular properties of ice and various types of ship-ice interaction processes. Therefore, many researchers have conducted to estimate ice loads more accurately. The ice loads can be classified into two categories; global ice load and local ice load, relating to the contact area. The global ice load can be referred as the load regarding longitudinal strength of the hull, motion or vibration of a hull. Contrary to the global ice load, the local ice load is the load acting on particular shell plating and structure members, resulting in damage and deformation (Choi and Jeong, 2008).

To estimate the ice loads, researches have been conducted in various ways such as full-scale measurement tests (Cheon et al., 2014), model tests (Jeong et al., 2015), and numerical analysis (Lubbad and Loset, 2011). Without sufficient analytic methods, the ice load data measured from the full-scale measurement test can provide valuable information for estimating the ice loads.

The objectives of the thesis are to estimate the local ice load acting on a vessel in ice-covered waters during 2016 Arctic voyage and compared with 2015 ice load data. In this thesis, two different approaches are considered to calculate local ice loads from strain gauge data. Strain gauge sensors were installed on the inner hull platings and at the transverse frames of ARAON's bow section. The first approach is to calculate concerning ice pressures using the influence coefficient method and the second approach is analyzed regarding shear forces acting on transverse frames.

The other objective of this study is to present the feasibility of fiber optic sensors. So far, the data obtained from full-scale ice field trials are obtained from electrical strain gauge sensors. These are usually affected by the electromagnetic interference, the wet and dirty corrosive environments on a vessel. Basically, the gauges have been well over-coated with recommended guidelines, but it is possible that gauges and protection system will suffer from long-term fatigue or environmental degradation. As a result, electrical strain gauge sensors are not entirely suitable for obtaining reliable information. Fiber optic sensors can overcome these problems. They are not affected by the electromagnetic interference that may be experienced onboard

a vessel. The optical sensors are also unaffected by the wet and dirty conditions are able to withstand low temperatures or corrosive environments. Using strain data measured from fiber optic sensors, local ice load is calculated, and the results are compared to those from electrical strain gauges. Estimating the local ice load and the possibilities of the fiber optic sensor presented in this thesis will be useful for future studies.

1.2 Organization of the Thesis

The remainder of this thesis is organized as below. In **Chapter 2**, an ice load measurement system is provided. In particular, the fiber optic sensor that can measure strains is introduced, and the advantages of these sensors are touched on.

In **Chapter 3**, it is explained about Arctic ice field tests and measurement of ice load data. For the full-scale measurement, the ARAON was instrumented with several different sensors. The ice load data was gathered using strain gauge and fiber optic sensors inside the shell plating and at some transverse hull frames. In relation to them, this chapter shows an arrangement of sensors in details.

In **Chapter 4**, two different approaches to estimate the local ice load from measured ice load data from electrical strain gauge sensors are introduced. In the analysis of ice load data, the concept of 'event' is applied to understand the characteristics of ship-ice interaction processes and to extract peak ice loads. The results calculated by two different approaches are described. The local ice loads estimated from 2016 Arctic voyage are compared to those from 2015 Arctic voyage. In particular, the shear forces acting on the transverse frames are compared to the calculated results from ice pressures to evaluate whether the second approach of using measuring shear strains can be an alternative method.

The possibility of fiber optic sensors for the future use is also discussed. The analysis is being made to compare the fiber optic sensors with the traditional electrical strain gauge sensors. In particular, the stresses calculated from the single gauge and rosette gauge are presented and local ice loads are estimated using the measured data from fiber optic sensors to compare with those results from electrical strain gauges.

In **Chapter 5**, conclusions and recommendations for further studies are mentioned.

Chapter 2 Ice Load Measurement System

2.1 Electrical Strain Gauge Sensors

The strain gauge is known as one of the most critical sensors of the electrical measurement technique. The strain gauge (sometimes referred to as a strain gage) is a sensor whose resistance varies with applied forces. When external forces are applied to a particular area, stress and strain are the results. Stress is defined as the internal resisting forces, and strain is defined as the displacement and deformation that occur. The strain gauge has a structure such that a grid-shaped sensing element of thin metallic resistive foil is put on a base of thin plastic film and is laminated with a thin film as shown in Fig. 2-1. Generally, the sensing element of the strain gauge is made of a copper-nickel alloy foil. The alloy has a rate of resistance change proportional to strain with a specific constant.

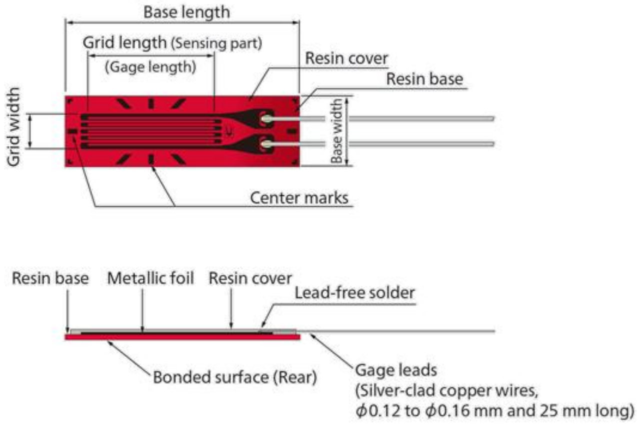

Fig. 2-1 Structure of a strain gauge

The principle of a strain gauge is that when bearing mechanical elongation or contraction, most metals undergo a change in electric resistance. The strain gauge applies this principle to strain measurement through the resistance change.

Strain gauge sensors can be categorized as various types as shown in Fig 2-2. In general, 1-axis single gauge(Fig. 2-2(a)) and 3-axis rosette gauge(Fig. 2-2(c)) are used to measure strain data. The type of sensor is changed depending on the purpose of a test. However, it is necessary to measure three strains at a particular point to completely define the strain field, such as estimating the ice load on the shell plating. In short, to estimate the local ice load acting on the hull plating, 3-axis gauge should be installed. For the ARAON's full-scale measurement tests, however, 1-axis and 3-axis rosette gauge have been used for the measurement of strains data.

The strain gauge sensors are currently being used in many industrial fields because of the various advantages of the electrical strain gauge sensor. However electrical strain gauges have limitation. As mentioned before, when forces are applied to sensors, the resistance varies with applied forces. Due to the change of resistance value, many factors make electrical strain gauges unstable for measuring strains on the inner hull plates for a long time. In addition, these sensors are not able to handle electrically noisy environments as well as wet and corrosive environments. So, it is essential to apply an alternative sensor to measure more accurate strain data.

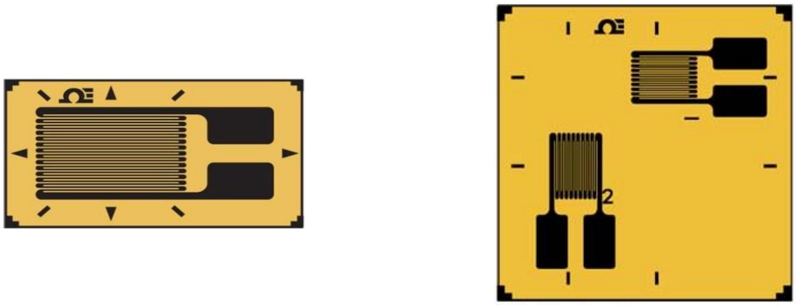

(a) 1-Axis strain gauge (b) 90° biaxial rosette

(c) 3-Element 45° strain rosette (d) 45° Planar strain rosette

Fig. 2-2 Types of strain gauge sensors

2.2 Fiber Optic Sensors

2.2.1 Structure of Fiber Optic Sensor

Fiber optic sensors are a fiber-based technique that uses optical fibers to detect certain quantities such as mechanical strain or temperature, concentrations of chemical species, acceleration, rotations, pressure, vibrations, and displacements.

A fiber optic sensor is composed of three parts, the core, the cladding, which has different refractive indexes, and the jacket. Figure 2-3 shows the structure of a typical fiber optic cable. The core of most fiber optic cables is made of pure glass and is generally a cylindrical rod of dielectric material. Light propagates mainly along the core of the fiber optic. The cladding layer is formed of a dielectric material with an index of refraction. The index of refraction of the cladding material is less than that of the core material.

The cladding is generally made of glass or plastic. Cores and claddings of fiber optic cables might be made from plastic, which is not as clear as than glass but plastic is more flexible and easier to handle maintenance. The cladding executes such functions as decreasing loss of light from core into the surrounding air, decreasing scattering loss at the surface of the core, protecting the fiber from absorbing the surface contaminants and adding mechanical strength(Jones, 1988). The jacket is made from a polymer(PVC, plastic) to protect the core and the cladding from physical damage. Additionally, the jacket has several important attributions, including bending ability, abrasion resistance, static fatigue protection, toughness, moisture resistance, and ability to be stripped. For a single fiber optic cable, The diameters of the core, cladding, and jacket are of 8~10, 125, and 250 μm, respectively (Table 1).

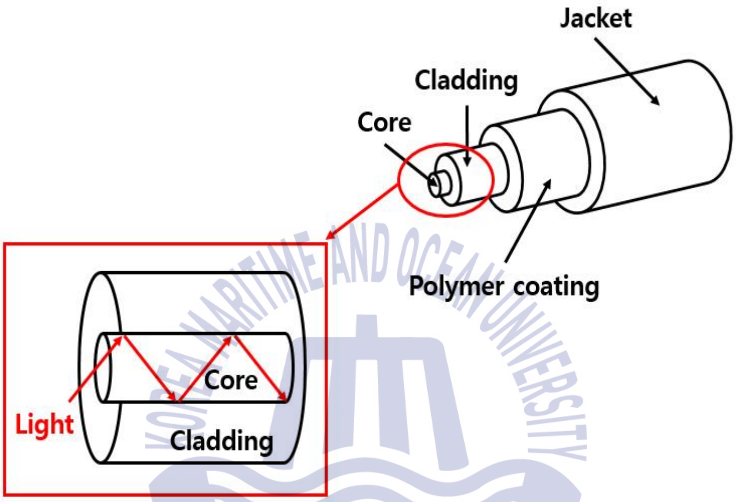

Fig. 2-3 Structure of fiber optic sensor

Table 1 Material and diameter of a single fiber optic cable

	Material	Diameter (μm)	
Core	SiO_2, GeO_2	8~10	material of higher refractive index
Cladding	SiO_2	125	material of lower refractive index
Jacket	Polymer, Acrylate	250	Protecting core and cladding

2.2.2 Basic Features of Fiber Optic Sensor

The light-guiding principle along the core is based on the “total internal reflection”. The angle at which total internal reflection occurs is called the critical angle of incidence. At any angle of incidence, higher than the critical angle, light is totally reflected back into the glass medium. In short, the difference on densities between the core and the layer enables the cables to act based on the total internal reflection principle, which states that the light striking a boundary between two components will be reflected without any loss in light energy. The reflected light is then transmitted to a sensor/detector that converts the light energy into an electrical signal.

Like with any other technology, there are both advantages and disadvantages using fiber optic sensor. The advantages include their small size, resistance to electromagnetic interference and high sensitivity. On the other hand, some of its problems are their high cost and unfamiliarity. But its super advantages completely overshadow its disadvantages. Fiber optic sensors are the excellent alternative sensor for measuring, and they offer many advantages over conventional electric sensors as below.

1) Fiber optic sensors are lightweight and this is of great importance in case of engineered structures.
2) Fiber optic sensors are of smaller size as compared to the conventional sensors.
3) Also, fiber optic sensors consume less power as compared to the conventional sensors.
4) Along with this, these sensors show high resistance to electromagnetic interference as compared to their conventional sensors.

5) Fiber optic sensors are usually embedded in objects and due to this, these sensors can gain access to areas which till date remain inaccessible with the aid of conventional sensors.
6) Also, these sensors are accurate over a higher dynamic range as compared to the conventional sensors.
7) Fiber optic sensors show greater environmental ruggedness ad compared to the traditional sensors.

2.3 Fiber Bragg Grating Sensor for Measuring Strain

Fiber Bragg Grating (FBG) technology is one of the most popular options used in various applications for strain or temperature measurements due to their simple manufacture as well as the relatively strong reflected signal. Basically, FBG sensors are formed by a periodic modulation of the index of refraction of the fiber core along the longitudinal direction.

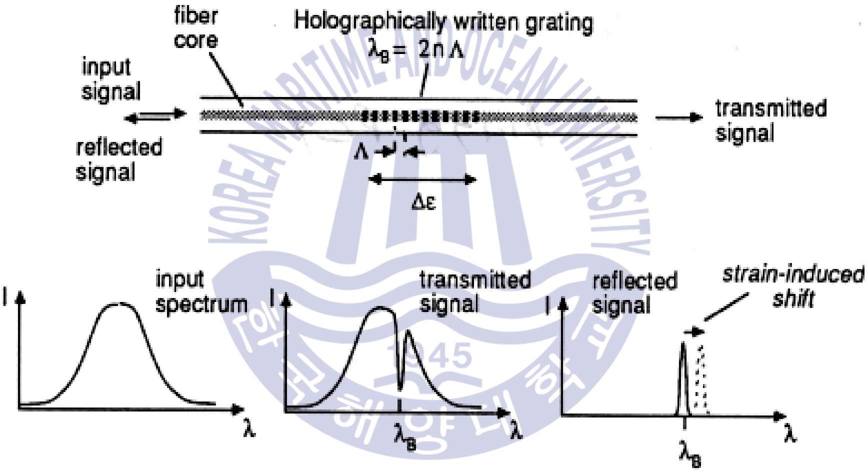

Fig. 2-4 Transmission and reflection spectra of a fiber bragg grating

Bragg diffraction occurs for electromagnetic radiation whose wavelength is the same order of magnitude of the atomic spacing when incident upon a crystalline material. In this case, the radiation is scattered in a specular fashion by the atoms of the material and experiences constructive interference in accordance with Bragg’s law. Bragg’s law describes the condition for constructive interference from several crystallographic planes of the crystalline lattice separated by a distance d.

$$2d\sin\theta = n\lambda \tag{1}$$

where θ is the incident angle, n is an integer, and λ is the wavelength. A diffraction pattern is obtained by measuring the intensity of the scattered radiation as a function of the angle θ. Whenever the scattered waves satisfy the Bragg condition, it is observed a strong intensity in the diffraction pattern, known as Bragg peak. After the inscription of the grating into the fiber’s core, due to the periodic modulation of the index refraction, light guided along the core of the fiber will be weakly reflected by each grating plane by Fresnel effect. The reflected light from each grating plane will join together with the other reflections in the backward direction. This addition may be constructive or destructive, depending on whether the wavelength of the incoming light meets the Bragg conditions of Eq. (1).

$$\lambda_B = 2n_{eff}\Lambda \tag{2}$$

Eq. (2), which is known as the Bragg reflection wavelength, is the peak wavelength of the narrowband spectral component reflected by the FBG, where the Bragg wavelength (λ_B) and FBG is a function of the effective refractive index of the fiber (n_{eff}) and the periodicity of the grating length (Λ). The bandwidth of this reflection depends on several parameters, particularly the grating length.

FBG is essentially a sensor of strain and temperature, but many other measurements can be made to impose perturbation on the grating resulting in a shift in the Bragg wavelength which can then be used as a parameter transducer. Therefore, many researchers can obtain measurements of strain, temperature, pressure, vibration, displacement, etc.

$$\triangle\lambda_B = \lambda_B\left[(1-P_e)\triangle\varepsilon + (\alpha+\xi)\triangle T\right] \tag{3}$$

where P_e is the strain optic coefficient, α is the thermal expansion coefficient and ξ is the thermo-optic coefficient. As shown in Eq.(3) the change in wavelength is not only dependent of effects that change refractive index and period, but also Bragg wavelength. Assuming that temperature change is minimal ($\triangle T = 0$), Eq. (4) is derived and strain can be measured through the change in Bragg wavelength.

$$\triangle\varepsilon = \frac{1}{(1-P_e)}\frac{\triangle\lambda_B}{\lambda_B} \tag{4}$$

Chapter 3 Arctic Ice Field Tests and Measurement of Ice Load Data

The icebreaking research vessel ARAON has performed the full-scale measurements in the Antarctic and Arctic Seas in 2010, 2011, 2012, 2013, 2015 and 2016. The instrumentation system that can collect ice load data has been slightly changed whenever the full-scale measurement test was conducted. The characteristics of tests and types of instrumentation system are summarized in Table 2. When a full-scale measurement test is performed, the following data can be measured. First, ice load data is measured using strain gauges, fiber optic sensors and a motion sensor and GPS as an integrated measurement system. The local ice load can be estimated with strain gauge sensors and fiber optic sensors. The local ice load means the sum of local ice loads calculated from each strain gauge sensor installed at sub-region of shell plating. The global ice load can be estimated using a motion sensor. Second, video cameras are placed externally to confirm the impact timing of the hull and the ice, and the ice conditions. Third, EM-31 device is installed in the bow section of ARAON to measure ice thickness in real time. Finally, the necessary information about the ice, such as temperature, compressive strength, and salinity is collected from a field test.

Table 2 Instrumentation system during each full-scale measurement

	Local Ice Load				Global Ice Load		
	Strain gauge sensor		Fiber optic sensor		Motion sensor		
	Official	Transit	Official	Transit	Official	Transit	
2010	O	O	X	X	O	O	Arctic
2011	X	X	X	X	O	O	Arctic
2012	O	O	X	X	X	X	Antarctic
2013	X	O	X	X	X	X	Arctic
2015	X	O	X	X	X	O	Arctic
2016	X	O	X	O	X	O	Arctic

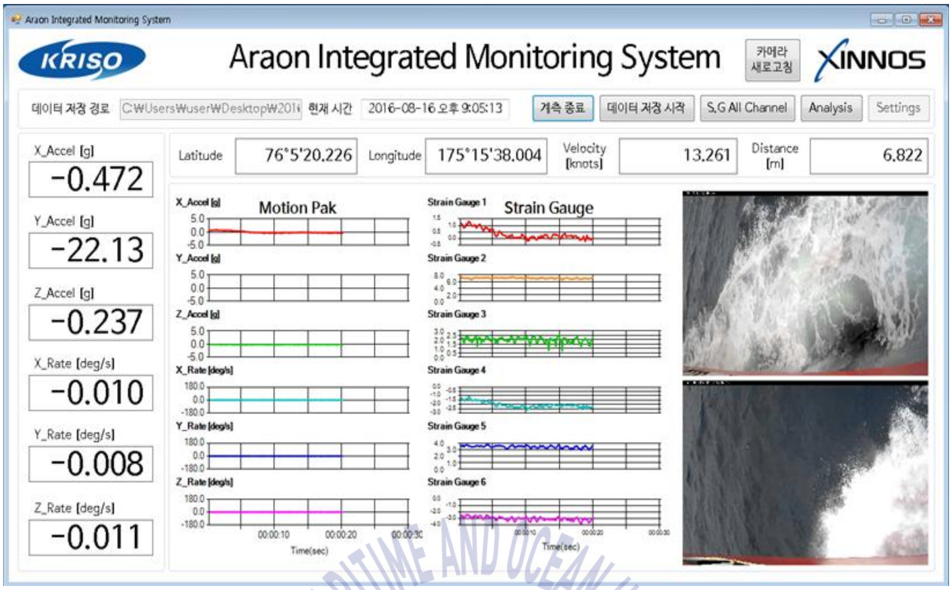

데이터 저장 경로 C:₩Users₩user₩Desktop₩201
현재 시간 2016-08-16 오후 9:05:13

X_Accel [g] -0.472
Y_Accel [g] -22.13
Z_Accel [g] -0.237
X_Rate [deg/s] -0.010
Y_Rate [deg/s] -0.008
Z_Rate [deg/s] -0.011

Latitude 76°5'20.226
Longitude 175°15'38.004
Velocity [knots] 13.261
Distance [m] 6.822

Fig. 3-1 ARAON's integrated monitoring system (strain gauge, MotionPak Ⅱ, GPS, CCTV)

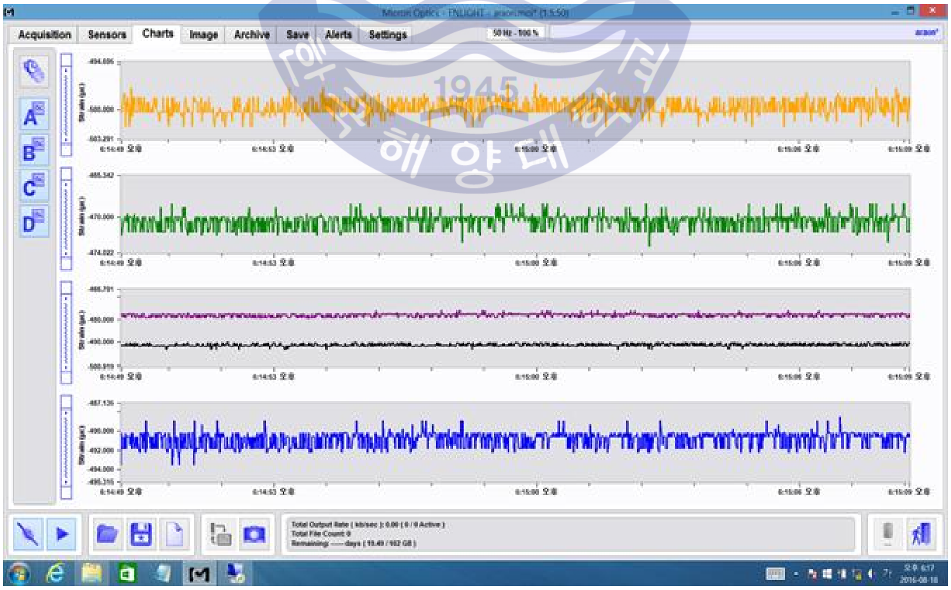

Fig. 3-2 A program for the strain measured by fiber optic sensors

For the full-scale measurement test during 2015 Arctic voyage, single gauge sensors were mainly installed inside the shell plating and 3-axis rosette gauges were used at some transverse hull frames to measure shear strain data. The ARAON's 2016 Arctic voyage was carried out in the Chukchi and East Siberian Seas as shown in Fig. 3-3. During 2016 Arctic voyage, the ARAON was instrumented with several different sensors which include strain gauges and fiber optic sensors. The location of strain gauge sensors has been slightly adjusted in 2016 from previously designated.

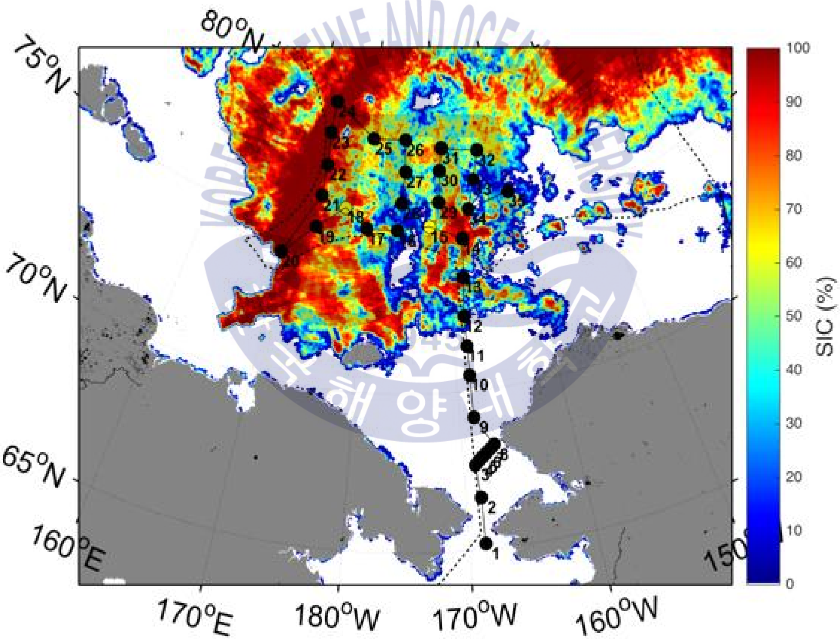

Fig. 3-3 ARAON's voyage in the Chukchi Sea and East Siberian Sea (August/September 2016)

Figure 3-4 shows the arrangement of sensors for the 2016 Arctic voyage. These were installed inside the shell plating and also at some transverse hull frames (frame No.102 ~ No.110 at the port side and frame No.106 ~ No.110 at the starboard side). The lower part of the second deck inside the bow thrust room was mostly covered to measure strain data. As shown in this Fig. 3-4, single gauge sensors and 3-axis rosette gauge sensors were used as the representative of electrical strain gauge sensors. The dotted markers indicate a single gauge sensor and cross markers are the locations of 3-axis rosette gauge sensors. The blanked cross markers show the locations of rosette gauges for measuring shear strains at the transverse hull frames. In addition to strain gauge sensors, red lines show the locations of fiber optic sensors which were newly applied from frame No.105 to frame No.110 at the shell plating. In the port side, a total of 8 single gauge sensors and 20 rosette gauge sensors were installed inside shell plating and also at the transverse frames as shown in the Fig. 3-4(a). Additionally, 5 fiber optic sensors were installed in the port side. In the starboard side (Fig. 3-4(b)), only 12 3-axis rosette gauge sensors were installed inside shell plating because of limited workspace. A total of 104 channels for strain gauges and 5 channels of fiber optic sensors could be recorded at the same time. Figure 3-5 shows the installed strain gauge sensors both the shell plating and the transverse frame. Figure 3-6 shows the fitted fiber optic sensor on the inner shell plating and the measurement equipment.

The global ice load is measured based on the whole-ship motions in six degrees of freedom. The motion data in six degrees of freedom were measured using the inertial measurement system “MotionPak II”(Lee et all, 2018). Fig. 3-7 shows the installation location of the inertial measurement system. It was installed on the back plane of an H-beam which supports the stairway from the main deck to the engine room.

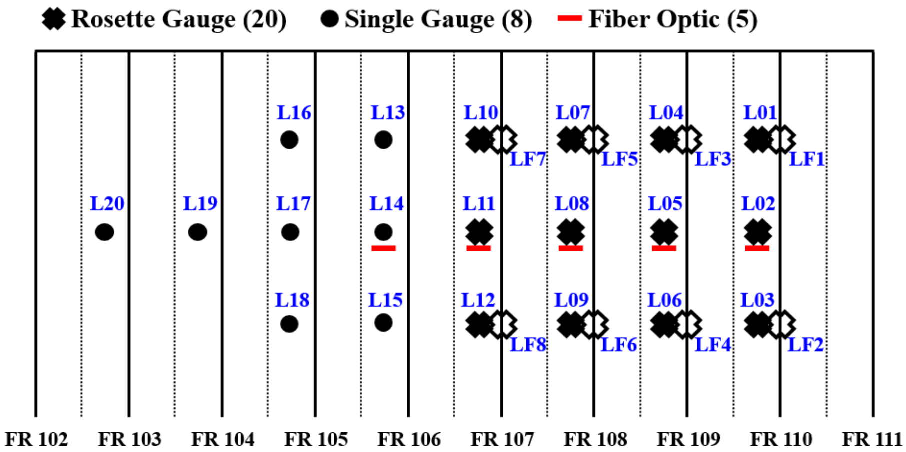

(a) Port side

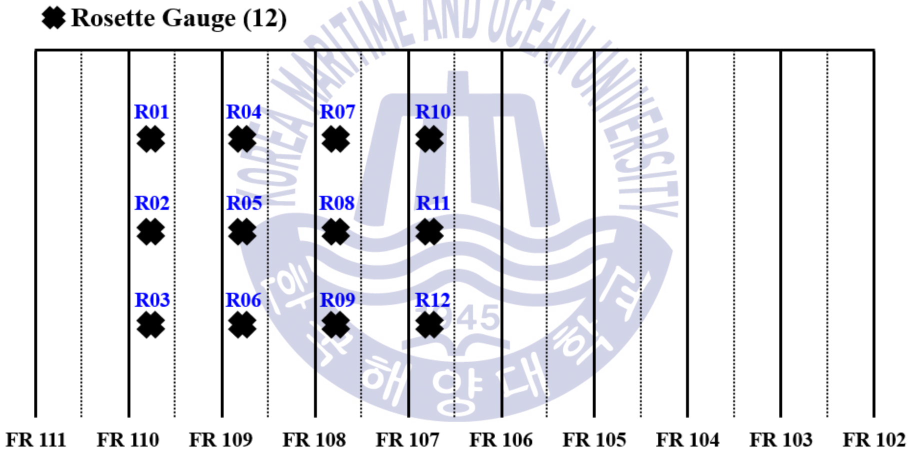

(b) Starboard side

Fig. 3-4 Location of installed strain gauge and fiber optic sensors during 2016 Arctic voyage (a) port side (b) starboard side

Fig. 3-5 Strain gauge sensors installed on the shell plating and at the transverse frame

Fig. 3-6 Fiber optic sensor installed on the inner shell plating and the measurement equipment

Fig. 3-7 MotionPak installed in the engine room

Fig. 3-8 ARAON’s 2016 Arctic voyage

Chapter 4 Analysis of Ice Load Data

4.1 Analysis Procedures of Ice Load Data

4.1.1 Calculation Method for Stresses according to Types of Sensor

As mentioned before, the icebreaking research vessel ARAON has been instrumented with strain gauges for the ice field measurements. However, each time the ice field measurements are conducted, the type of strain gauges, the location, and number of strain gauges are slightly changed, and the procedures of estimating local ice load are complicated. Furthermore, there is a difference in calculating the stresses depending on the type of strain gauge. To accurately estimate the local ice load acting on the vessel, it is necessary to confirm the strain data measured from both single gauges and 3-axis rosette gauges. In this section, the methods that can calculate the stresses using single gauge and rosettes gauge data and the difference of results depending on the methods are explained.

In case of a single gauge, Eq. (5) known as the uniaxial Hooke’s law is used for calculating stress. Basically the strain is proportional to the stress whithin the elastic limit

$$\sigma_x = E \times \epsilon_x \tag{5}$$

where ϵ_x is the measured strain in the x-axis direction and E is the modulus of elasticity. When a single gauge is installed, eq. (5) is used. It means that the strain of y and 45° direction is not needed to be taken into account. Only the x-axis direction is mainly affected in determining the stress on the hull plating.

When a 3-axis rosette gauge is instrumented on the hull plating $(\epsilon_A, \epsilon_B, \epsilon_C)$, the von Mises equivalent stress equation is used for calculating stresses. Eq. (6) is an equation for the principle stresses in the orthogonal direction in a plane problem and Eq. (7) is called as the von Mises equivalent stress, where υ is the Poisson's ratio, σ_1 and σ_2 are the principle stresses, respectively.

$$\sigma_1, \sigma_2 = \frac{E}{2(1-\upsilon)}(\epsilon_A + \upsilon_B) \pm \frac{E\sqrt{2}}{2(1+\upsilon)}\sqrt{(\epsilon_A - \epsilon_C)^2 + (\epsilon_B - \epsilon_C)^2} \tag{6}$$

$$\sigma_{eq} = \sqrt{\sigma_1^2 + \sigma_2^2 - \sigma_1\sigma_2} \tag{7}$$

4.1.2 Influence Coefficient Method

The estimation of ice loads acting on a vessel is essential, but is complicated through the manipulation of strains. Ice loads can be estimated by using indirect methods from the measured strain data. Two approaches were used for the estimation of ice loads in this thesis. The first approach is the use of the influence coefficient method which tells how a force or displacement at a particular point influences a displacement or force at another position. It is presented here that the relationship between hull stresses and ice pressures in a location where strain gauges are installed. Fig. 4-1 shows the overall flow chart of ice load estimation procedures using the influence coefficient matrix. The influence coefficient matrix is determined numerically by finite element analysis of the structure. The structure of the ARAON's bow section was analyzed using a commercial FE software PATRAN. The unit pressure is applied to every position to obtain each element of influence coefficient matrix.

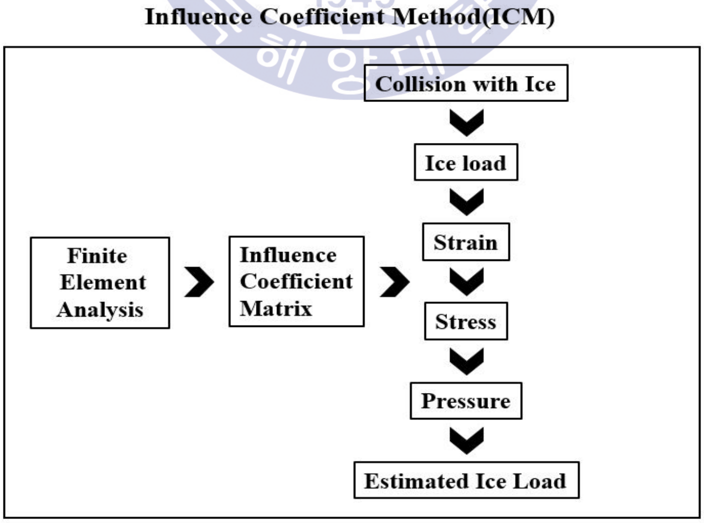

Fig. 4-1 Flow chart of the influence coefficient method

The measured strain data is converted to hull stresses using von Mises equivalent stress equation and ice pressure/ice load is calculated by using the influence coefficient matrix. The ice pressure/ice load calculated by the inverse estimation are regarded as the local ice load acting on the area in which one strain gauge is covered. The size of shell plating covered by one strain gauge is 800×500mm. When summing up the local ice loads calculated from each strain gauge, it is defined as the local ice load acting on the hull plating where all strain gauges are installed.

For example, for the 2016 Arctic voyage, a total of 20 strain gauges (both 1-axis and 3-axis rosette gauges) was installed at the port side. In case of this situation, the influence coefficient matrix was made of [20×20] elements. On the starboard side, the size of the influence coefficient matrix was [12×12] since 12 rosette gauge sensors were installed. The influence coefficient matrix is represented as $[C]$ in Fig. 4-2 and the inverse matrix $[C]^{-1}$ is used to calculate ice pressures by multiplying hull stresses. The procedure to calculate ice pressures and local ice load on hull plating is well described in previous studies (Choi et al., 2014; Kim, 2016).

$$\begin{Bmatrix} \sigma_1 \\ \sigma_2 \\ \sigma_3 \end{Bmatrix} = \begin{bmatrix} C_{11} C_{12} C_{13} \\ C_{21} C_{22} C_{23} \\ C_{31} C_{32} C_{33} \end{bmatrix} \begin{Bmatrix} P_1 \\ P_2 \\ P_3 \end{Bmatrix}$$

$$\Downarrow$$

$$\begin{Bmatrix} P_1 \\ P_2 \\ P_3 \end{Bmatrix} = \begin{bmatrix} C_{11} C_{12} C_{13} \\ C_{21} C_{22} C_{23} \\ C_{31} C_{32} C_{33} \end{bmatrix}^{-1} \begin{Bmatrix} \sigma_1 \\ \sigma_2 \\ \sigma_3 \end{Bmatrix}$$

Fig. 4-2 Relationship between the hull stresses and ice pressures

4.1.3 Shear Strain Data in Hull Frames

Since 2015 Arctic ice trials, 3-axis rosette gauges have been installed at transverse frames for measuring shear strains. In this thesis, the shear strain data gathered at the locations of frames during 2016 Arctic voyage is used for calculating the shear force along the frame.

In 2016 Arctic ice trials, 3-axis rosette gauges were only installed at the port side to measure shear strain data. A total of 8 rosette gauges was installed at four frames (No.107 ~ No.110). Fig. 4-3 shows the schematic diagrams for analyzing shear forces on the frame. As shown in this figure, two 3-axis rosette gauges were installed at the upper part and the lower part of each frame. Shear forces can be calculated by the difference of shear strains in the frame.

Generally 3-axis rosette gauge can measure normal strains in three directions, $(\epsilon_a, \epsilon_b, \epsilon_c)$, hence the Shear strains are calculated from the measurement data in two-dimensional Mohr’s circle diagram as in Eq. (8). Shear stresses are simply calculated by Eq. (9).

$$\gamma_a = -(2\epsilon_b - \epsilon_a - \epsilon_c) \tag{8}$$

$$\tau = G \cdot \gamma_a = \frac{E \cdot \gamma_a}{2(1+\upsilon)} \tag{9}$$

where E is the elastic modulus, γ_a is the measured shear strains, and v is the Poisson's ratio. Finally, shear forces are calculated by Eq. (10).

$$F_{shear} = k(\tau_1 - \tau_2)A \tag{10}$$

where τ_1 and τ_2 are shear stresses calculated from Eq. (9) at the upper and at the lower parts of the frame, respectively. A is the shear area where the shear stresses are working on the frame (Fig. 4-3), and k is a factor that adjusts the shear area(A) depending on shape of the frame. In this thesis 1.0 is used for shear area factor temporarily.

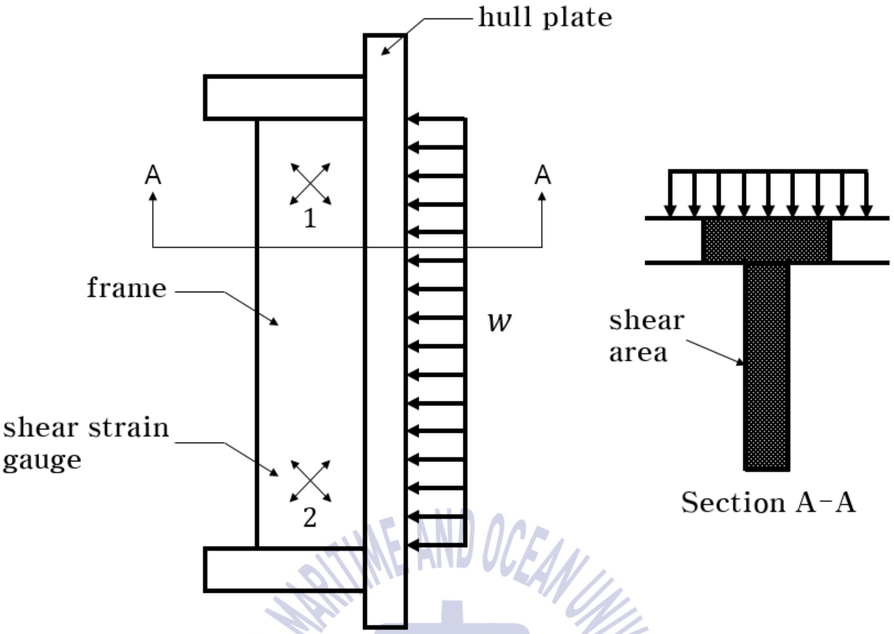

Fig. 4-3 Location of strain gauges at the frame of ARAON's bow section

Table 3 Calculated shear areas

Frame. No	Area (mm^2)
106	23,940
107 ~ 110	15,640

4.1.4 Concept of an Event and Peak Ice Load

To understand the characteristics of a ship-ice interaction process, it is useful to adopt the concept of an ‘event’ from which the peak ice load and collision speed can be defined. This concept is well described in the previous study(Min et al., 2016). When a ship collides with large ice feature, the speed of ship sharply decreases as ship penetrates into the ice. Contrary to decreasing ship speed, the ice load increases to a particular peak value and then ice fails. As shown in Fig. 4-4, the time history of local ice load estimated by summing pressures at the sensors can be divided into a series of events. It is possible to select one peak ice load and one incoming ship speed during each event. The ship speed was recorded from a GPS onboard the ARAON.

To obtain a meaningful data, it is needed to set a threshold for extracting a ship speed and peak ice load. The maximum value in an event is selected as the peak ice load. The threshold for peak ice load was set to 0.4 MN for 2016 ice load data. The value of 0.4 MN seems to be a little high while it is compared to 2015 ice load data(threshold value 0.04 MN for 2015 ice load data). The reason for this might be explained by comparing ice conditions in 2015 and 2016 seasons as shown in Fig. 4-7. And the threshold of peak ice load for 2012 Antarctica ice load data was set to 0.4 MN, as 2016 ice load data. The speed of the ship was selected as a speed of 0.5 sec ahead of the instance at which the peak ice load is achieved. Figure 4-5 shows the selected peak ice loads of each event.

Figure 4-6 shows the icebreaking procedure in the ice field measurement. When ARAON’s encounters an ice sheet, crushing occurs at the stern and the ship speed sharply decrease at the same time. Contrary to decreasing the ship speed, the contact area continuous to gradually increase to a particular peak value. After crushing with the ice sheet, the ice failure occurs. This procedure is repeatedly happened.

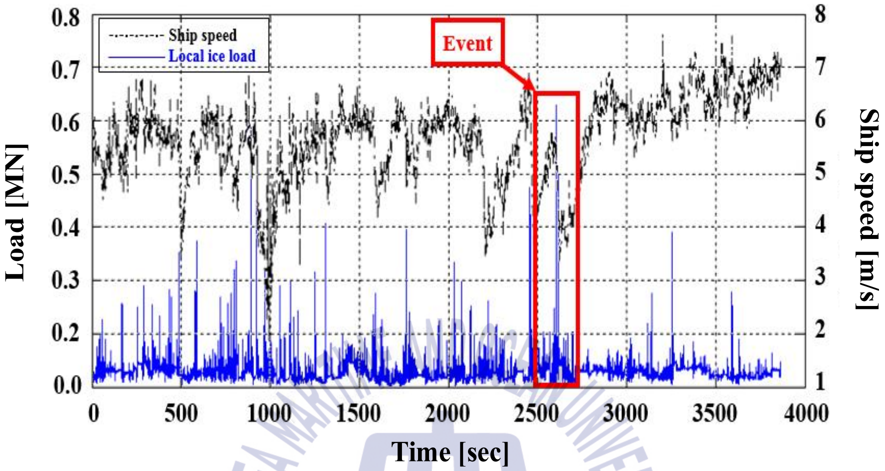

Fig. 4-4 Typical time histories of local ice load and ship speed

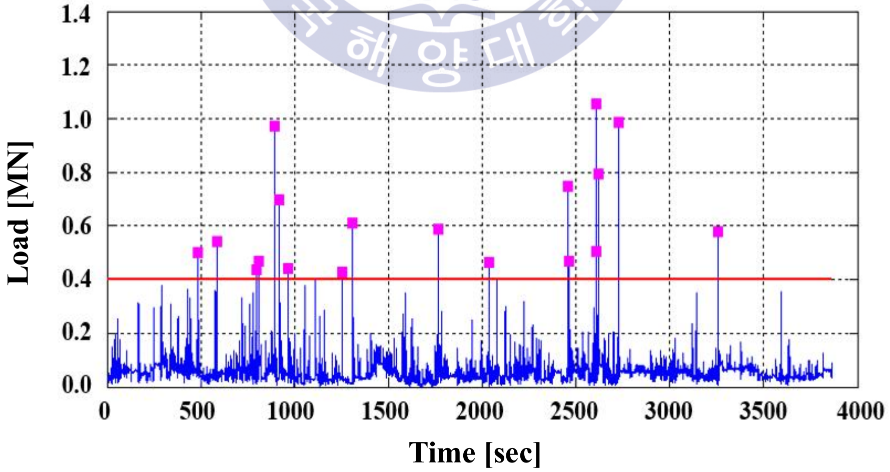

Fig. 4-5 Extraction of peak ice loads and minimum threshold of 0.4 MN

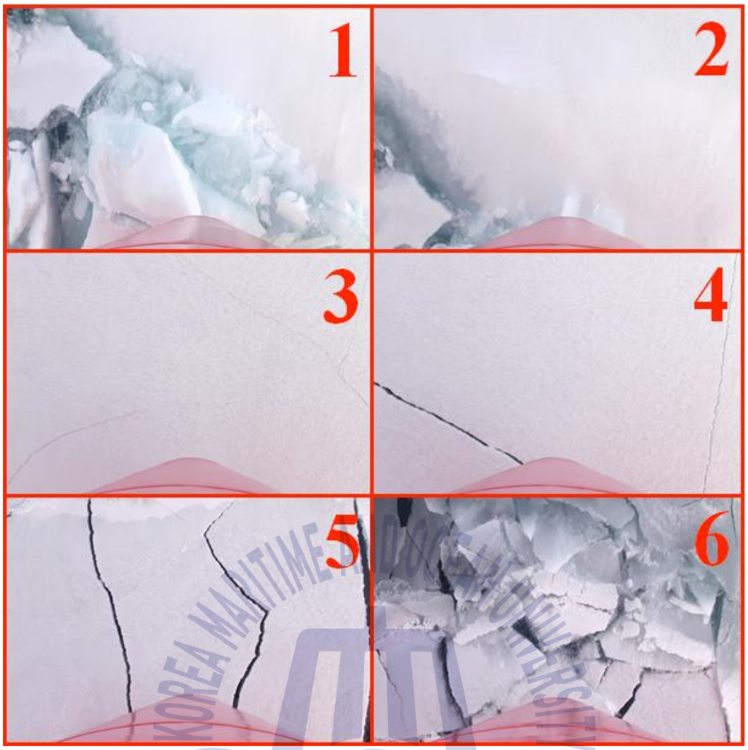

Fig. 4-6 Icebreaking procedures in the ice field measurement

(a) (b)

Fig. 4-7 Typical ice conditions during (a) 2015 Arctic voyage (b) 2016 Arctic voyage

4.2 Estimation of Local Ice Load by Influence Coefficient Method and Calculation of Shear Force

4.2.1 Local Ice Load by using Influence Coefficient Method

During 2016 Arctic voyages, local ice loads acting on ARAON's bow section were measured by using electric strain gauges and fiber optic sensors which were installed on the inner hull plates and transverse frames of bow section. In this section, a total of 32 data groups were analyzed for estimating the local ice loads from 2016 full-scale measurement data. Firstly, the local ice load was estimated from strain data measured on the port side and the starboard side of ARAON's using the influence coefficient matrix.

Figures 4-8 and 4-9 show the local ice loads estimated from the hull plating of port side and from starboard side analyzing No. 19 data group. Figure 4-10 presents the sum of local ice loads from the port side and the starboard side. It is unreasonable to compare local ice loads estimated from both side since the number of strain gauges installed on the port side and the starboard side are different. However, peak values are found to occur at a similar instance. Additionally, in order to confirm the relationship of peak ice loads and ship speed, all the events were extracted from the 2016 ice load data and ship speed data. A total of 424 events were found based on the threshold value of 1.0 MN and the maximum value of peak ice loads was 3.60 MN from No. 1 data group. As shown in Fig. 4-11, peak values are distributed with speed range(3~7 m/s). The ice load data was gathered under normal operating condition. This is in stark contrast to official teats which were conducted to break thick ice at low ship speed.

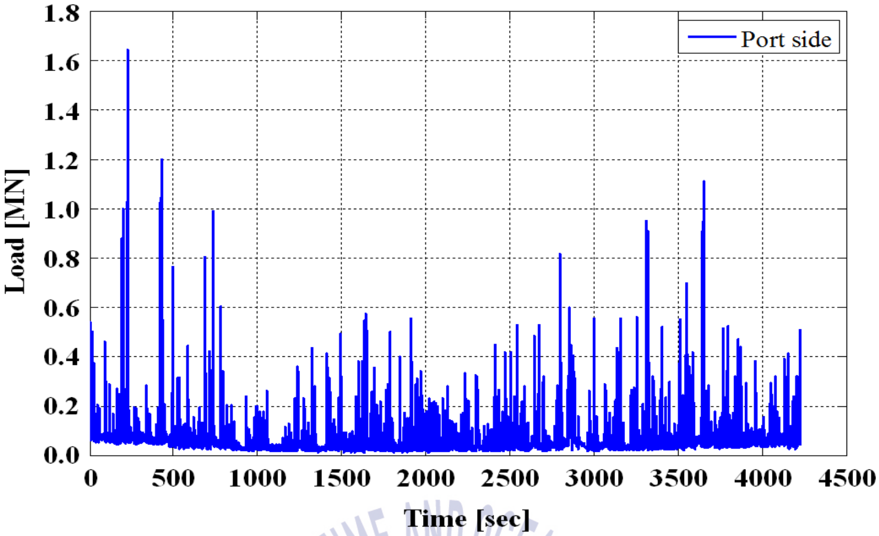

Fig. 4-8 Sum of ice loads acting on the port side (2016 data group No.19)

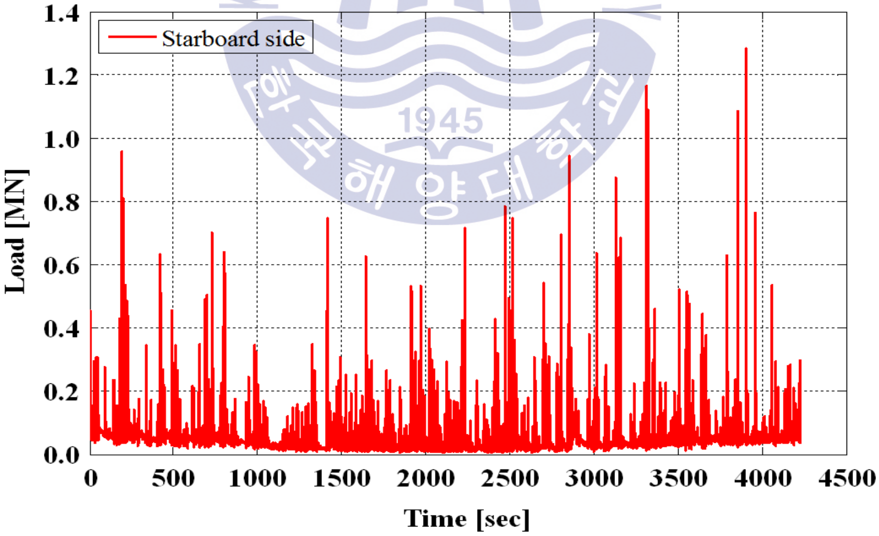

Fig. 4-9 Sum of ice loads acting on the starboard side (2016 data group No.19)

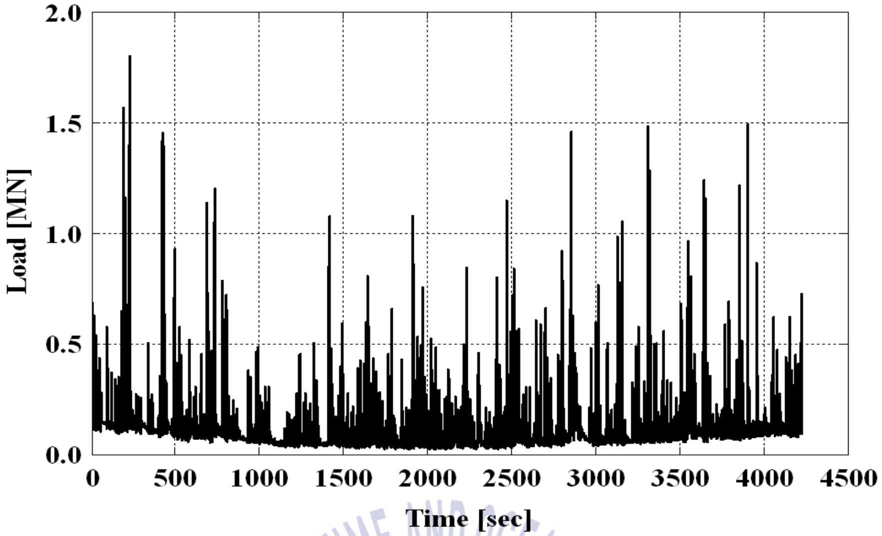

Fig. 4-10 Sum of ice loads from the both sides (2016 data group No.19)

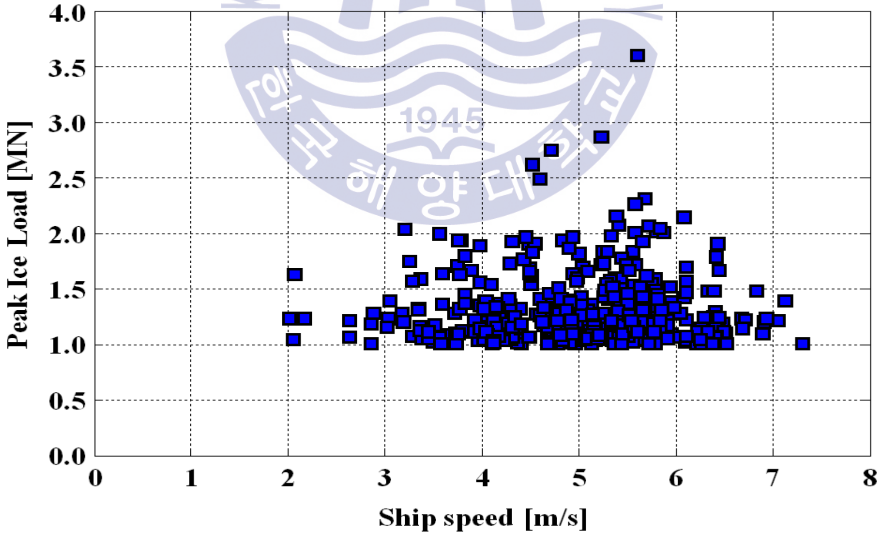

Fig. 4-11 Peak ice loads vs. ship speed acting on hull plating for all 32 data groups of 2016 AROAN's Arctic field measurement

In 2015 Arctic voyage, a total of 30 data groups were gathered and analyzed for estimating the local ice loads from full-scale measurement data. In the analysis process of 2015 ice load data, strain data in the direction of the y-axis and 45° was assumed as zero since the ARAON was equipped with only single gauges on the inner hull plating. Figure 4-12 shows the location of strain gauges installed on the hull plating of the IBRV ARAON during 2015 Arctic voyage. On the port side, 24 single gauges and 10 rosette gauges were installed and 12 single gauges and 4 rosette gauges were installed on the starboard side. A total of 78 channels were used for measuring strain data at the same time in 2015 Arctic voyage.

Figure 4-13 presents the sum of local ice loads from the port side and the starboard side. Fig. 4-14 shows the extracted events from 2015 data groups. As a result, a total of 83 events were detected in all data groups, and the maximum/average values are 0.77 MN and 0.47 MN, based on 0.4 MN threshold. Tables 4 and 5 show the results of the comparison between the 2015 Arctic voyage and 2016 Arctic voyage. As compared to the results, the local ice loads estimated from 2016 ice load data are confirmed to be about 3 to 5 times larger than those from 2015 ice load data. This results can be explained by different environmental conditions and ice conditions of which the tests were conducted in 2015 and 2016.

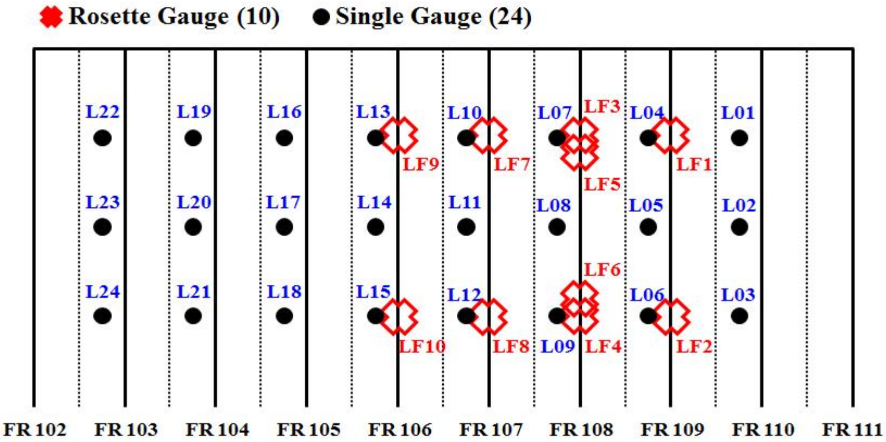

(a) Port side

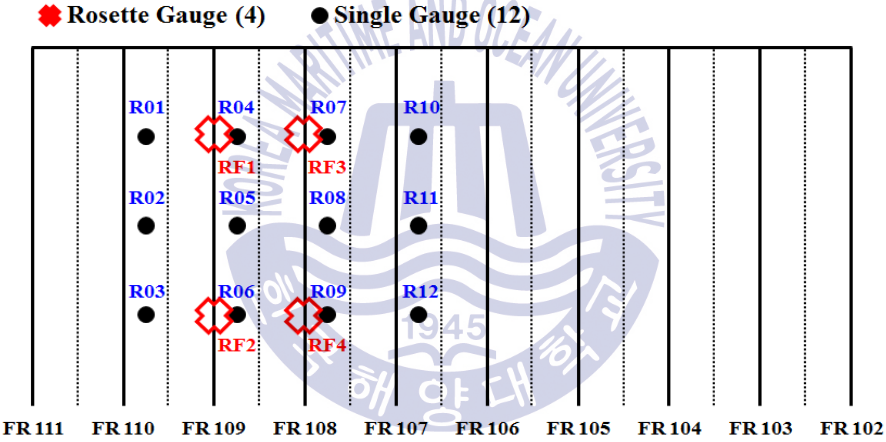

(b) Starboard side

Fig. 4-12 Location of installed strain gauges on the hull plating of the ARAON during 2015 Arctic voyage (a) port side (b) starboard side

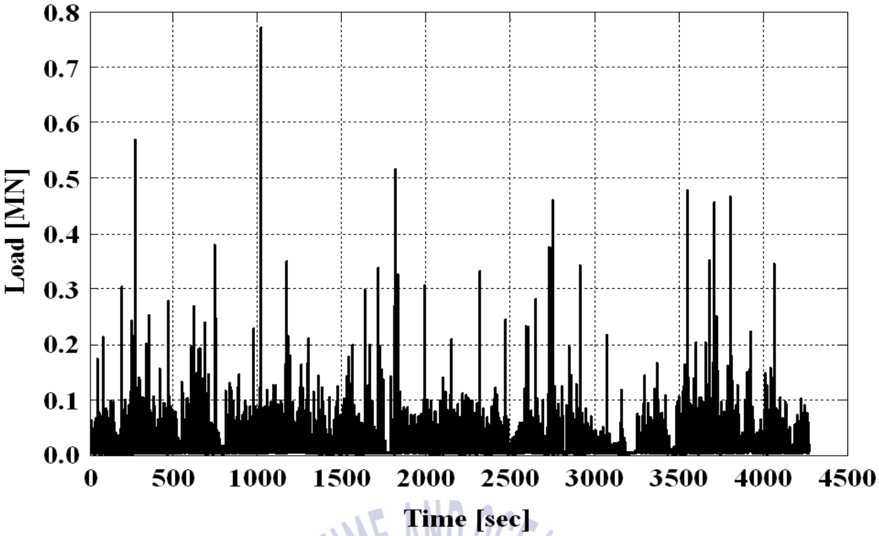

Fig. 4-13 Sum of ice loads from the port side and the starboard side (2015 data group No.5)

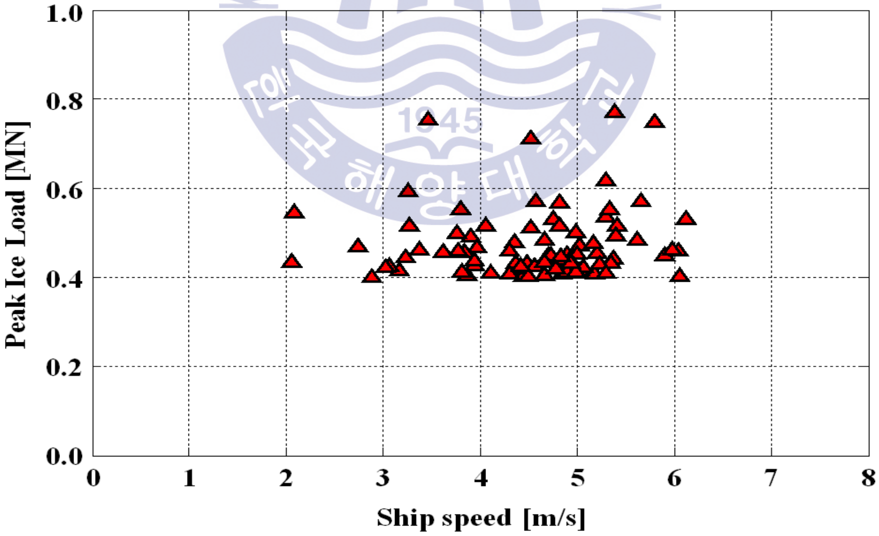

Fig. 4-14 Peak ice loads vs. ship speed acting on hull plating for all 30 data groups of 2015 AROAN's Arctic field measurement

Table 4 Comparison of events extracted from 2015 ice load data and 2016 ice load data (Data group 1-16)

Data Group	2015 Arctic voyage			2016 Arctic voyage		
	Number of event	Max. of peak ice loads [MN]	Aver. of peak ice loads [MN]	Number of event	Max. of peak ice loads [MN]	Aver. of peak ice loads [MN]
1	-	-	-	29	3.60	1.40
2	5	0.57	0.45	28	2.75	1.43
3	3	0.47	0.44	-	-	-
4	10	0.57	0.47	5	1.94	1.60
5	8	0.77	0.52	8	1.91	1.29
6	1	0.42	0.42	22	1.99	1.23
7	5	0.55	0.47	36	2.31	1.27
8	24	0.75	0.46	33	1.93	1.24
9	5	0.52	0.47	36	2.86	1.38
10	3	0.75	0.54	-	-	-
11	1	0.45	0.45	-	-	-
12	-	-	-	12	1.64	1.19
13	-	-	-	3	1.33	1.16
14	-	-	-	5	1.27	1.12
15	1	0.53	0.53	10	2.26	1.42
16	1	0.50	0.50	6	1.88	1.26

Table 5 Comparison of events extracted from 2015 and 2016 ice load data (Data group 17-32)

Data Group	2015 Arctic voyage			2016 Arctic voyage		
	Number of event	Max. of peak ice loads [MN]	Aver. of peak ice loads [MN]	Number of event	Max. of peak ice loads [MN]	Aver. of peak ice loads [MN]
17	5	0.71	0.54	14	2.03	1.38
18	-	-	-	15	2.01	1.37
19	1	0.46	0.46	28	1.80	1.26
20	2	0.45	0.44	14	1.60	1.20
21	3	0.59	0.48	33	2.07	1.23
22	1	0.42	0.42	18	1.66	1.23
23	1	0.43	0.43	2	1.19	1.10
24	-	-	-	3	1.30	1.14
25	-	-	-	-	-	-
26	1	0.55	0.55	1	1.31	1.31
27	-	-	-	9	1.84	1.31
28	2	0.41	0.41	2	1.57	1.33
29	-	-	-	14	1.94	1.31
30	-	-	-	18	2.14	1.28
31				3	1.46	1.25
32				17	2.15	1.43

4.2.2 Local Ice Load from Shear Strain Data in Hull Frames

Strain gauges were installed not only on the inner hull plating but also at transverse frames of ARAON's bow section during 2016 Arctic voyage. This section aims to analyze shear strain data and to compare two different approaches each other. The strain gauge data measured from 2015 Arctic voyages were also examined to verify whether there is a similar trend in estimated local ice loads. To compare the results from two approaches, a sub-region of the shell plating where shear strains were measured was considered in the analysis(Fig. 4-15). As mentioned before, the shear forces acting on the transverse frames were calculated by using shear strain data and shear stress/force equations. Ice pressures and ice loads acting on hull plating were derived by using the influence coefficient matrix.

Previous researchers showed that ice loads could be estimated by using shear gauges on the hull frame of ships such as CANMAR KIGORIAK, SOYA and Manhattan, but details of calculation procedures to analyzed the shear data were not released (Ghoneim et al., 1984; Takimoto et al., 2006; Suominen et al., 2013). In 2015 Arctic voyage, the use of strain gauges to measure shear strain data at transverse frames was attempted on the icebreaking research vessel ARAON, as the alternative method to estimate local ice load acting on hull plating. However several data groups were damaged or not retrieved because of gauge failures in the processes of measuring data.

A total of 32 data groups were analyzed for estimating the local ice loads from 2016 full-scale measurement data. Figures 4-16 and 4-17 show the local ice loads estimated from shear forces along the transverse frames and from the hull plating ice pressure analyzing No. 9 data group. The maximum load acting on hull plating is 1.34 MN, which is a little higher than the maximum load acting on the frames(1.06 MN). Local ice loads calculated by two approaches show a resonable agreement in general as shown in Fig. 4-20.

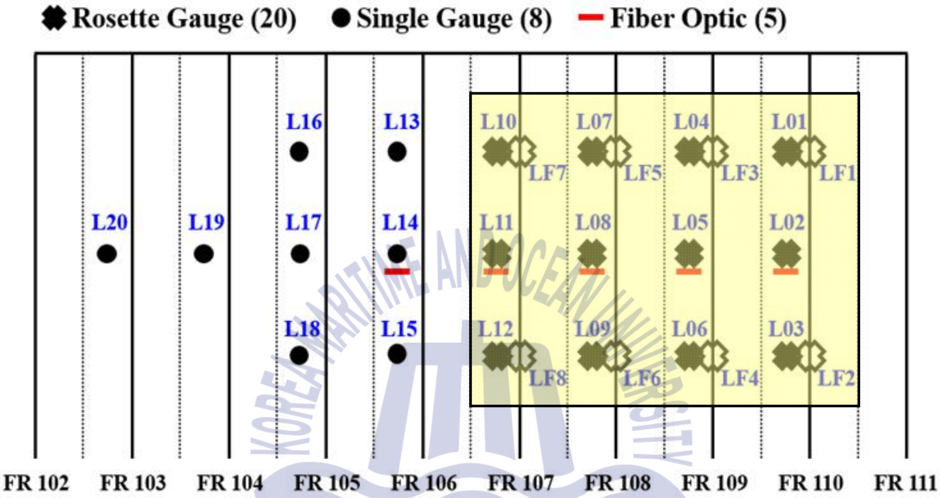

Fig. 4-15 Sub-region of the shell plating where shear strains were measured

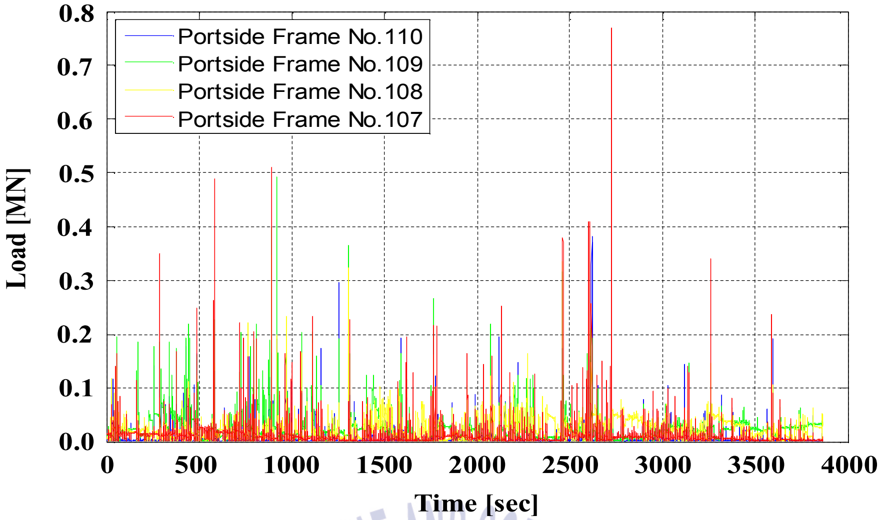

Fig. 4-16 Shear forces acting on each frame

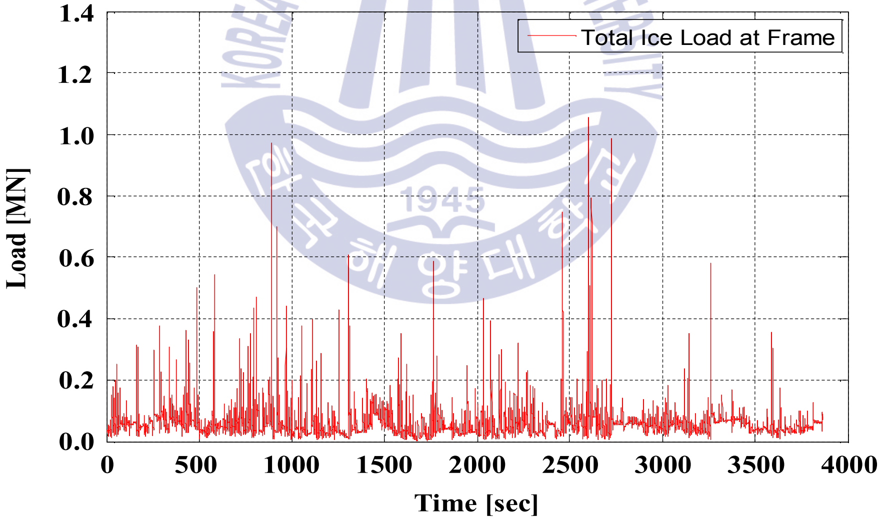

Fig. 4-17 Sum of shear forces acting on a frame

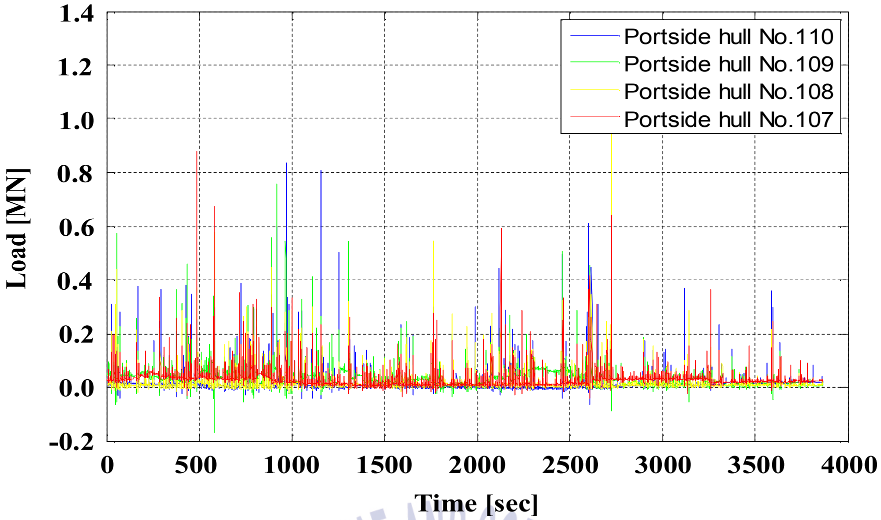

Fig. 4-18 Ice loads on hull plates corresponding to each frame

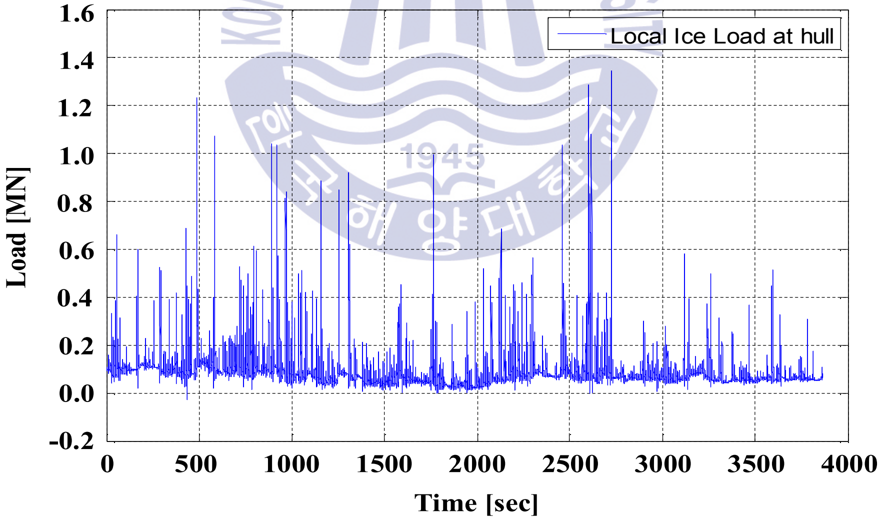

Fig. 4-19 Sum of ice loads on hull plating

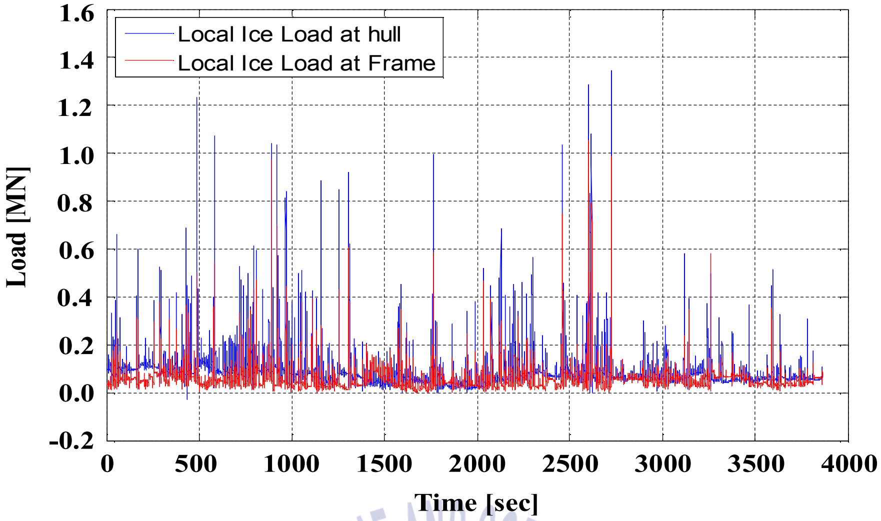

Fig. 4-20 Comparison of local ice loads acting on hull plating and at transverse frame

To understand the characteristics of peak ice loads acting on transverse frames and loads acting on hull plating, all the events were analyzed to extract the peak ice load and corresponding ship speed from the 2016 ice load data and GPS data. Based on the threshold value of 0.4 MN, a total of 267 events were found, and the maximum value of peak ice loads was 1.45 MN at 4.52 m/s(Fig. 4-21). By analyzing the events extracted from the local ice loads on hull plating, a total of 871 events were found and the maximum value of peak ice loads 2.41 MN at 4.52 m/s. As shown in Fig. 4-22, the peak ice loads acting on the hull plating section are a little higher than those on the transverse frames. The average value of peak ice loads acting on the frame is estimated at 85% of loading on the hull plating. Additionally, the peak ice loads data from the full-scale measurement shows accumulation within a particular ship speed range(3~7 m/s).

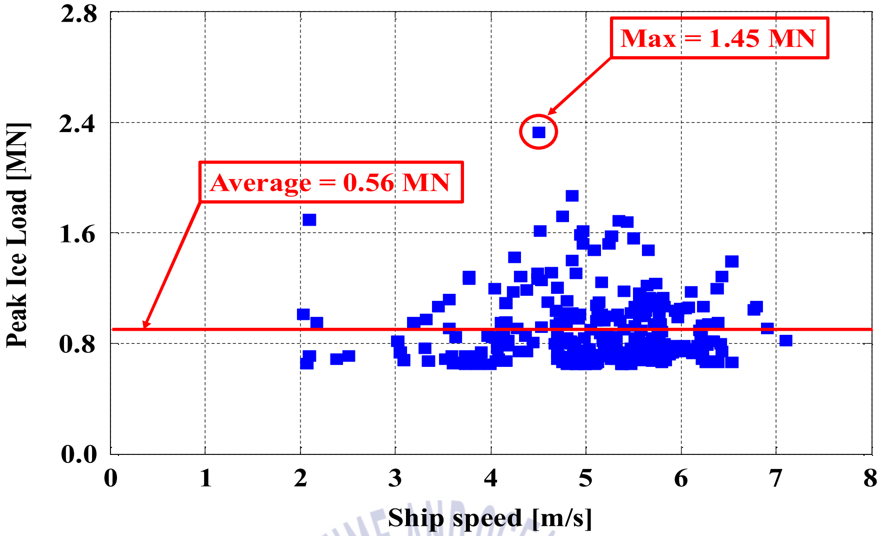

Fig. 4-21 Peak ice loads vs. ship speed from transverse frames for all 32 data groups of 2016 ARAON's Arctic field measurement

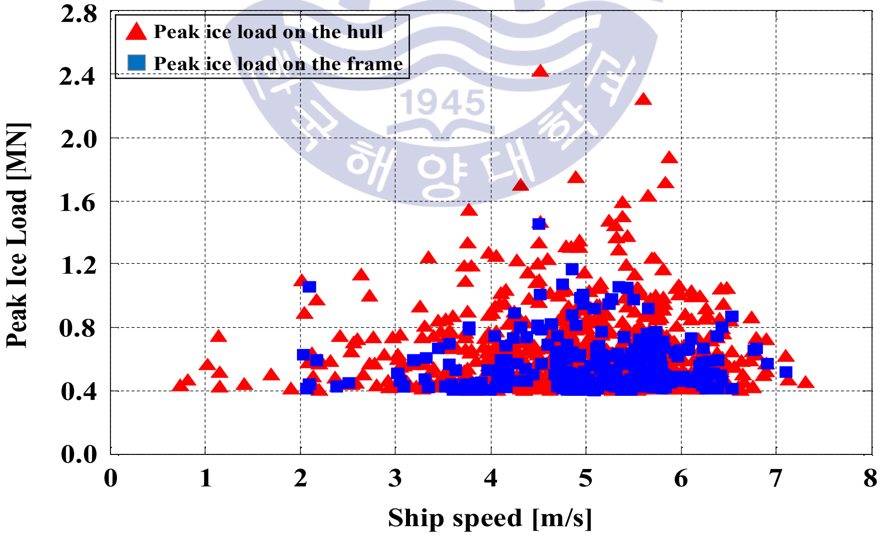

Fig. 4-22 Peak ice loads vs. ship speed from hull plating and from transverse frames for all 32 data groups of 2016 ARAON's Arctic field measurement

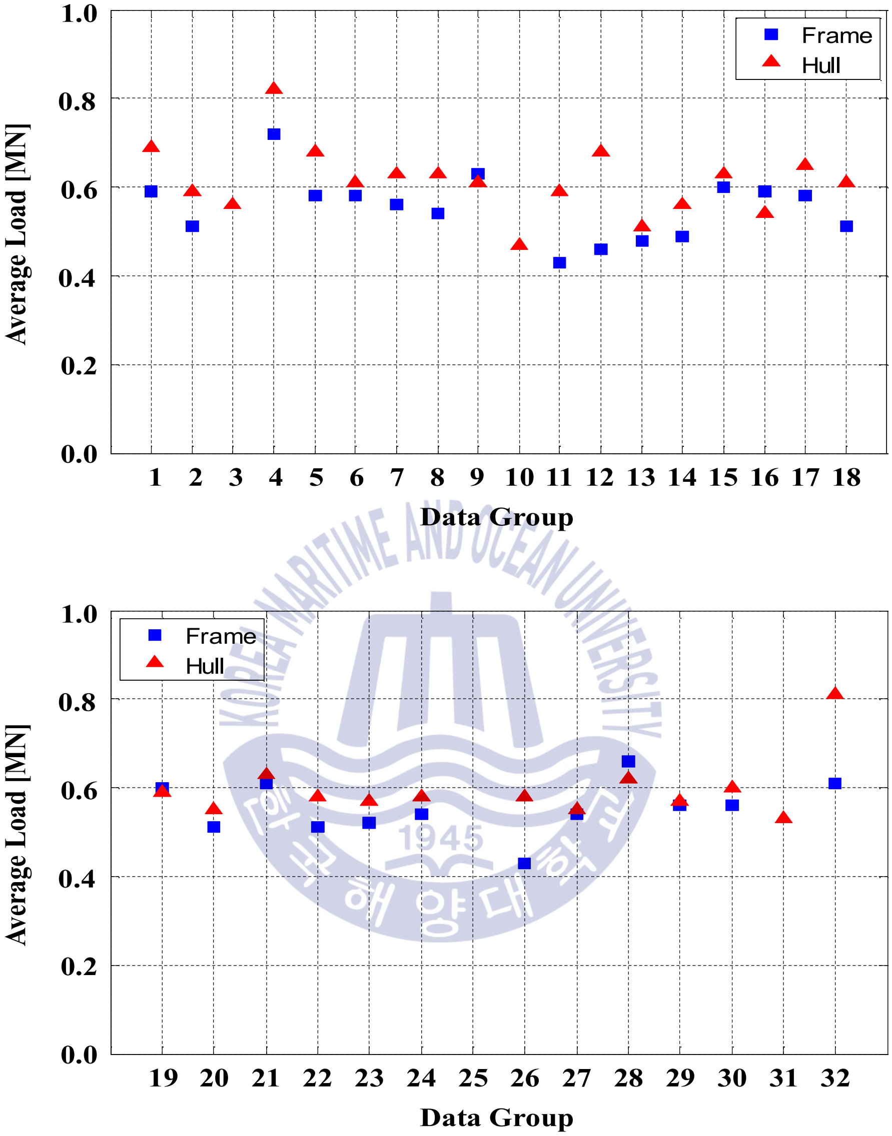

Fig. 4-23 Average of peak ice loads from hull platings and from transverse frames for all 32 data groups of 2016 ARAON's Arctic field measurement

By analyzing 2015 shear strain data based on the threshold value(0.04 MN), a total of 120 events were found, and the maximum value is 0.11 MN at 4.46 m/s ship speed(see Table 6). The peak ice loads extracted from calculated local ice loads were distributed within 0.04 ~ 0.11 MN and 3 ~ 7 m/s range. It is possible to compare both results quantitatively since the environmental conditions including ice properties, and measurement locations were not precisely same when the measurement tests were conducted. However, those results show that there is a similar distribution trend of peak ice load vs. particular ship speed range.

Table 6 Comparison of events extracted from shear data in 2015 and 2016 Arctic voyages

	2015 Arctic voyage	2016 Arctic voyage
Number of events	120	267
Maximum value of peak ice loads	0.05 MN	0.56 MN
Average value of peak ice loads	0.11 MN	1.45 MN

4.3 Estimation of Local Ice Load from Fiber Optic Sensors

4.3.1 Comparison of Stresses Calculated from Single and Rosette Gauge Sensors

To compare the calculated stresses from a fiber optic sensor with those from a strain gauge, in this study, only sub-region of the shell plating where fiber optic and strain gauge sensors are installed is considered(see Fig. 4-24). A total of 32 data groups are analyzed. In the process of checking anomalies in the gathered data groups, abnormal signals were found at L5 strain gauge as shown in Fig. 4-25. The measured signals of the y-axis and 45° directions indicate abnormal signals compared with the signal of x-axis direction. In case of L5 strain gauge, the strain signals y-axis and 45° directions are excluded, and only x-axis direction is considered. In the other hand, there are no irregular signals in all the data groups. Figure 4-26 shows the example of strain signals from fiber optic sensors.

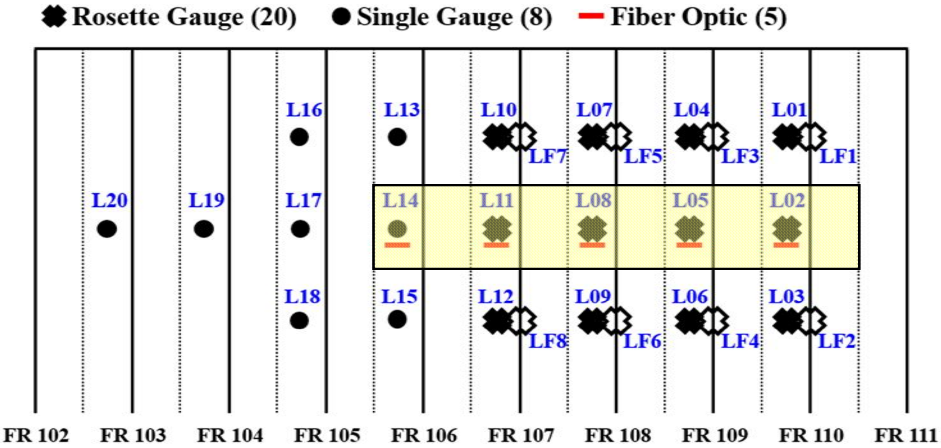

(a) Port side

Fig. 4-24 Sub-region of the shell plating where fiber optic sensors were installed

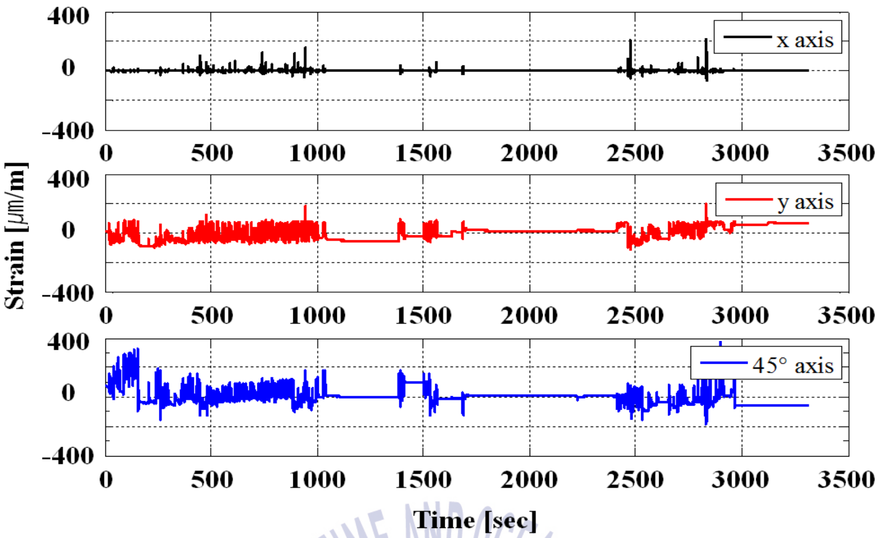

Fig. 4-25 Example of abnormal signal patterns (L5 strain gauge)

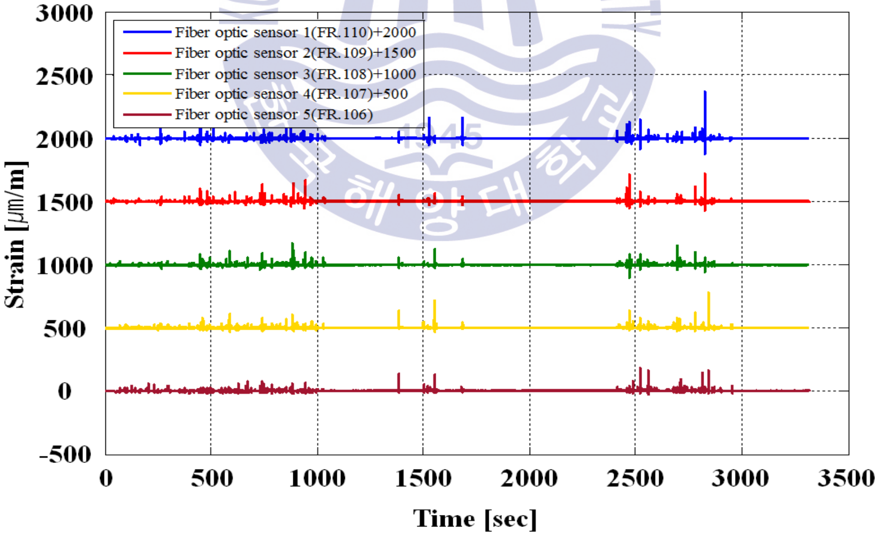

Fig. 4-26 Example of strain signal from fiber optic sensors. Constant offsets have been added to the time series for visuality

To compare the performance of the fiber optic sensor with the strain gauge, three different methods to calculate stresses were considered. The first method is only x-direction strain data measured from one sensor, and the x-direction strain data is applied to Hooke’s law to calculate the stress. The second method is to calculate stresses using the von Mises equivalent stress equation. In this case, two strains in three directions are needed. The x direction strain was measured from a sensor and other directions(y-axis and 45°) were assumed as zero. The third method is for calculating the stress by using actual three direction strains which were measured from a 3-axis rosette gauge and using the von Mises equivalent stress equation.

It is expected that since two sensors cannot be installed in the same location, there are slight differences in two sensors. However, the sensors were installed at close as possible to measure strains at almost same location. Figure 4-27 shows the results by analyzing No. 5 data group. The fiber optic sensor that measures one direction strain(x-axis) corresponds to the first case and the second case. In case of the rosette gauge, the second and third methods were used for calculating stresses. The first figure of Fig. 4-27 represents the stresses calculated using the von Mises equivalent stress equation. The maximum values are 88.37 MPa and 59.13 MPa respectively. The second figure of Fig. 4-27 represents the calculated stress applying the x direction strain to the Hooke’s law. The maximum values are 74.75 MPa and 45.23 MPa respectively. Although the same data is used, the results show that there is same difference depending on the methods of calculating stresses.

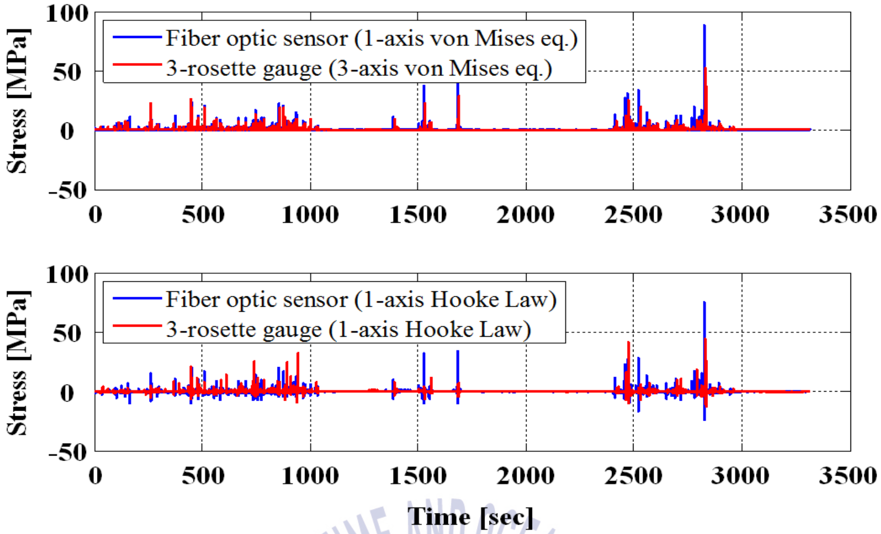

Fig. 4-27 Comparison of stresses calculated by two methods of using fiber optic sensor data and 3-rosette strain gauge data

The results of all data groups gathered in 2016 Arctic voyage are summarized in Table 7 and Table 8. The strains data used to calculate stresses was measured in the strain gauge(L2) and the fiber optic sensors, which were installed in the hull plating of frame No. 110. In case of the 3-axis rosette gauge, the calculated stress values using the Hooke's law are substantially lower than the calculated stress values using the von Mises equivalent stress equation. In addition, in case of the fiber optic sensor, the assessed stress values using the Hooke's law are approximately 80% of the calculated stress values using the von Mises equivalent stress equation. It can be inferred that the strain data in the direction of the y-axis and 45° is affecting the stress values in the calculation process. Furthermore, assuming that the strain data in the directions of the y-axis and 45 degree is zero, the von Mises equivalent stress equation can be an alternative method on behalf of the Hooke's law which only uses the x-axis direction strain data.

Table 7 Comparison of the stresses calculated by von Mises eq. and Hooke's law (Data Group 1-16)

Data Group	Fiber optic sensor		3-rosette gauge	
	3-axis von Mises eq.	1-axis Hooke's Law	3-axis von Mises eq.	1-axis Hooke's Law
1	99.08	83.80	69.50	65.88
2	62.97	53.26	51.67	41.70
3	47.02	39.77	36.98	61.12
4	64.50	54.55	56.14	31.42
5	88.38	74.75	59.13	45.23
6	73.79	62.41	49.98	70.69
7	133.71	113.09	98.02	94.30
8	118.33	100.08	81.57	76.41
9	85.02	71.91	67.50	66.35
10	25.01	21.15	20.58	18.55
11	56.72	47.97	47.84	19.19
12	33.91	28.68	23.22	22.37
13	41.36	34.98	34.25	23.20
14	61.54	52.05	30.57	25.67
15	107.74	91.12	85.30	49.97
16	47.91	40.52	32.57	37.85

Table 8 Comparison of the stresses calculated by von Mises eq. and Hooke's law (Data group 17-32)

Data Group	Fiber optic sensor		3-rosette gauge	
	3-axis von Mises eq.	1-axis Hooke's Law	3-axis von Mises eq.	1-axis Hooke's Law
17	66.44	56.20	65.92	52.28
18	86.16	72.87	68.32	28.35
19	66.95	56.62	51.83	52.69
20	91.35	77.26	73.49	41.16
21	151.97	128.54	124.65	82.89
22	95.72	80.96	106.69	54.61
23	58.66	49.61	48.21	24.95
24	42.98	36.35	27.78	35.30
25	26.55	22.46	23.06	10.66
26	67.47	57.07	41.94	62.33
27	85.46	72.28	59.37	48.19
28	55.41	46.87	54.13	32.54
29	92.05	77.86	69.97	64.72
30	137.05	115.92	113.52	59.54
31	65.04	55.01	45.38	29.97
32	108.54	91.81	82.51	73.89

4.3.2 Comparison of Local Ice Loads by Fiber Optic and Strain Gauge Sensors

The objective of this part is to compare local ice loads estimated from fiber optic sensors with those determined from strain gauges. As mentioned above, only sub-region of the shell plating where fiber optic sensors were installed was considered in this analysis to compare two types of sensors each other. Firstly, two types of sensors are used to estimate ice pressures on the sub-region of the shell plating. Hull stresses are calculated by the von Mises equivalent stress equation, and the influence coefficient method is used for ice pressures. Finally, the local ice load can be calculated by multiplying the area of sub-region.

The No. 5 data group was analyzed for estimating the local ice loads from 2016 full-scale measurement data. Figures 4-28 and 4-29 show the calculated ice loads for each fiber optic sensor and the total sum of ice loads in time histories, analyzing No. 5 data group. Figures 4-30 and 4-31 show the calculated ice loads for each strain gauge(L02, L05, L0, L11, L14) and the total sum of ice loads, respectively. As shown in Fig. 4-29 and Fig. 4-31 the tendency to occur at peak ice values appears almost identical. The results of local ice loads estimated from two types of sensors show that the maximum value of the local ice load estimated from fiber optic sensors is 1.18 MN and the maximum value of the local ice load estimated from strain gauges is 0.90 MN. The maximum value estimated from strain gauges was approximately 76%, compared to the maximum value from optical sensors.

Although a slight difference between the two results occurred, it was inferred that fiber optic sensors were able to measure strain data more reliably than strain gauges in the harsh environments.

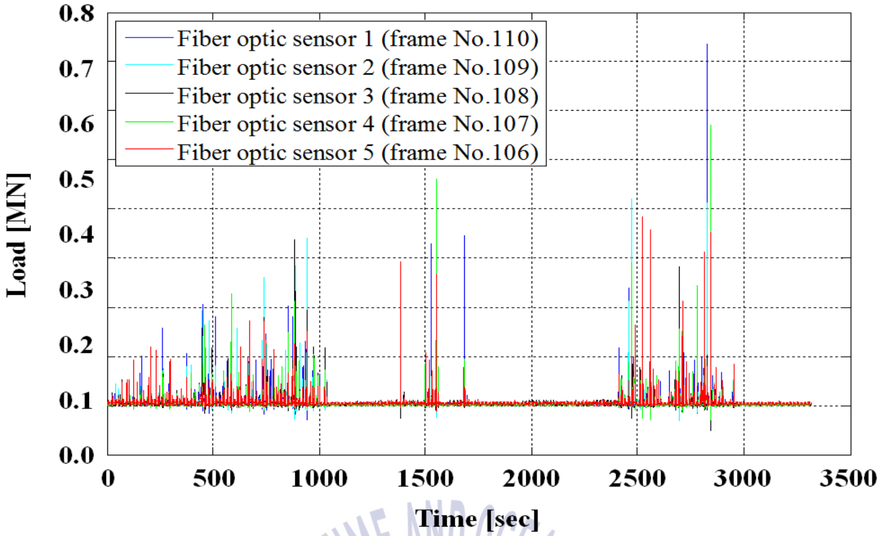

Fig. 4-28 Ice loads calculated from fiber optic sensors (No. 5 data group)

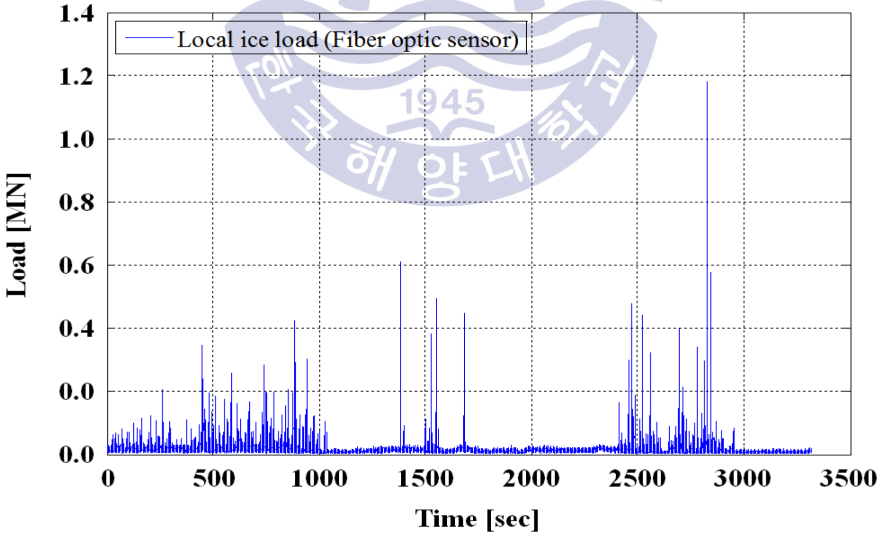

Fig. 4-29 Sum of ice loads calculated from fiber optic sensors (No. 5 data group)

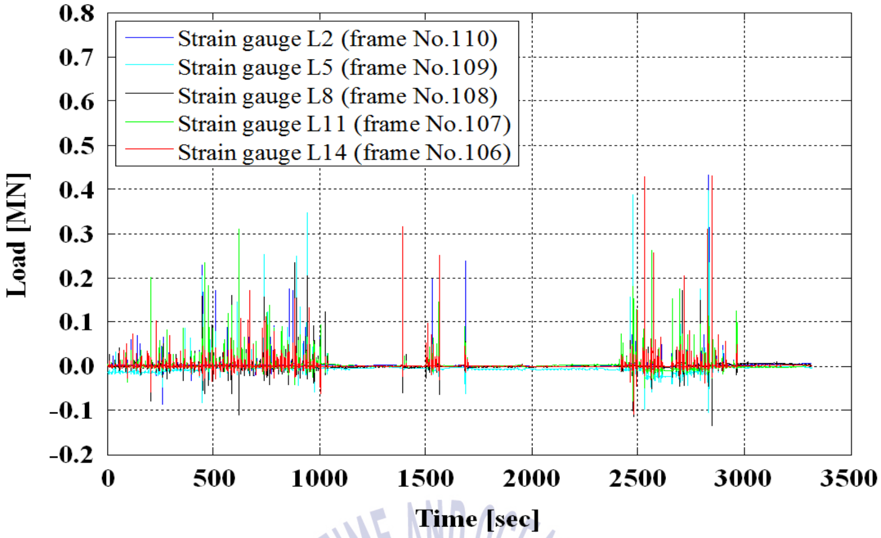

Fig. 4-30 Ice loads calculated from strain gauge sensors (No. 5 data group)

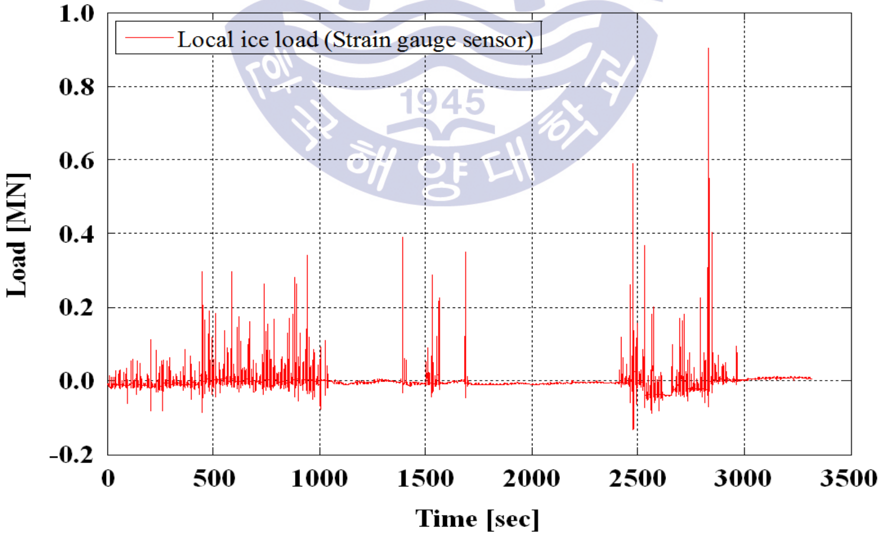

Fig. 4-31 Sum of ice loads calculated from strain gauge sensors (No. 5 data group)

To compare the characteristics of peak ice loads extracted from fiber optic sensors with peak ice loads extracted from strain gauge sensors. All the events were analyzed to obtain the peak ice loads from the 2016 ice load data. The threshold for peak ice load was set to 0.4 MN for the strain data measured in fiber optic sensors. The value of 0.4 MN is equal to the threshold value for peak ice loads acting on transverse frames from 2016 ice field measurement. Tables 9 and 10 show the number of events, the average and maximum values of peak ice loads estimated from both fiber optic and strain gauge sensors. Figures 4-32 and 4-33 show extracted peak ice loads and corresponding ship speed from ice load data measured in fiber optic and strain gauge sensors. In case of the fiber optic sensor, a total of 447 events were found, and the maximum and average values of peak ice loads were 1.32 MN and 0.59 MN respectively. By analyzing the events extracted from strain gauge sensors, a total of 299 events were found, and the maximum and average values of peak ice loads were 1.49 MN and 0.55 MN respectively. Those results are similar to the maximum value, and average value(1.45 MN and 0.56 MN) estimated from peak ice loads acting on transverse frames(2016 Arctic ice filed measurement)(Jeon et al., 2017). As a result of analyzing all data groups, peak ice loads extracted from fiber optic sensors are overall a little higher than those extracted from strain gauge sensors. But the average values are presented with similar results. And those peak ice loads are distributed within 0.04 ~ 0.15 MN and 3 ~ 7 m/s range.

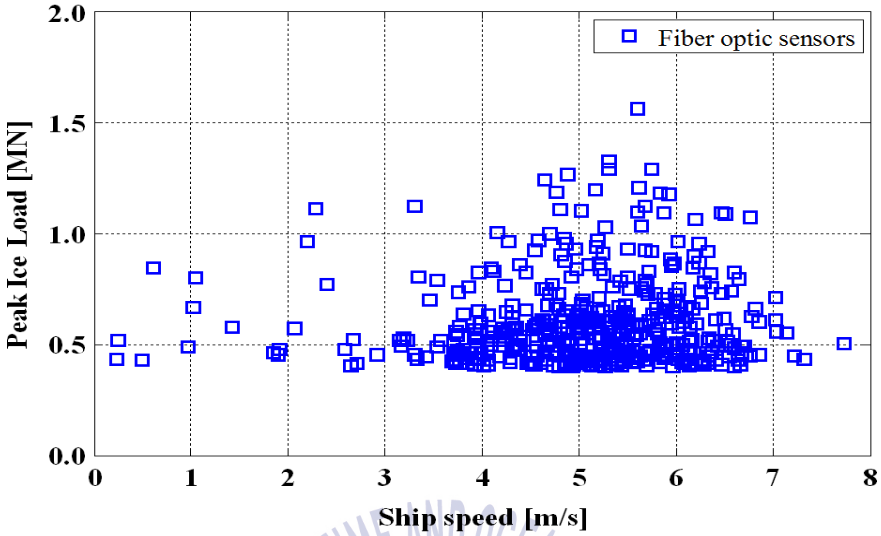

Fig. 4-32 Peak ice loads vs. ship speed from fiber optic sensors for all 32 data groups of 2016 ARAON's Arctic field measurement

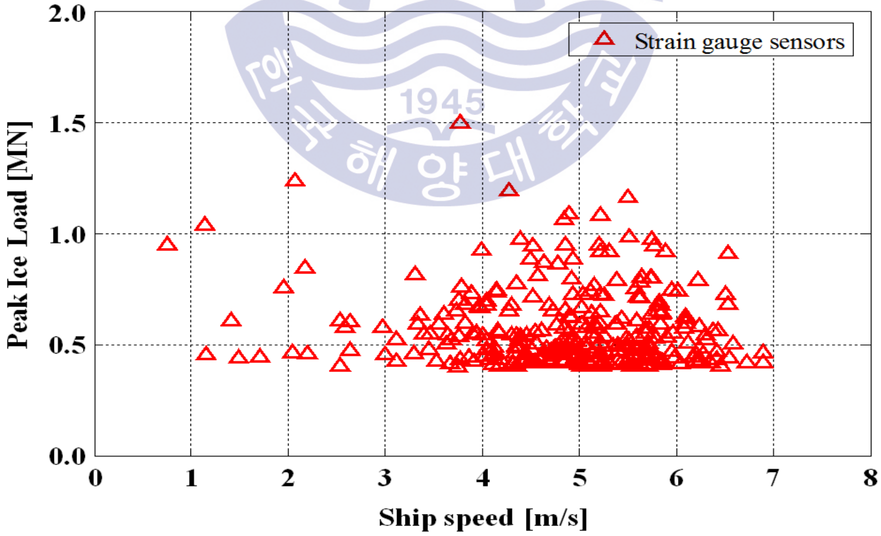

Fig. 4-33 Peak ice loads vs. ship speed from strain gauge sensors corresponding fiber optic sensors for all 32 data groups of 2016 ARAON's Arctic field measurement

Table 9 Comparison of events calculated from two different types sensors (Data group 1-16)

Data Group	Fiber optic sensor			Strain gauge sensor		
	Number of event	Max. of peak ice loads [MN]	Aver. of peak ice loads [MN]	Number of event	Max. of peak ice loads [MN]	Aver. of peak ice loads [MN]
1	24	1.10	0.63	23	0.94	0.60
2	25	0.97	0.51	14	0.68	0.51
3	2	0.69	0.54	1	0.69	0.69
4	5	1.19	0.71	4	1.05	0.59
5	9	1.18	0.59	4	0.90	0.61
6	21	1.11	0.63	16	1.20	0.62
7	35	1.56	0.59	27	1.05	0.59
8	31	1.10	0.65	20	0.84	0.53
9	27	1.29	0.64	21	0.87	0.55
10	1	0.41	0.40	-	-	-
11	1	0.48	0.47	1	0.43	0.43
12	4	0.83	0.56	2	0.60	0.54
13	-	-	-	-	-	-
14	6	0.63	0.52	1	0.44	0.44
15	6	0.92	0.73	7	0.75	0.60
16	10	1.11	0.61	5	0.63	0.55

Table 10 Comparison of events calculated from two different types sensors (Data group 17-32)

Data Group	Fiber optic sensor			Strain gauge sensor		
	Number of event	Max. of peak ice loads [MN]	Aver. of peak ice loads [MN]	Number of event	Max. of peak ice loads [MN]	Aver. of peak ice loads [MN]
17	20	0.95	0.55	6	0.61	0.51
18	14	1.09	0.62	10	1.14	0.58
19	21	1.00	0.59	15	0.71	0.54
20	18	1.18	0.65	15	0.92	0.56
21	35	1.32	0.60	26	1.17	0.56
22	26	1.12	0.53	21	0.99	0.53
23	7	0.93	0.54	3	0.76	0.54
24	7	0.82	0.62	4	0.48	0.44
25	-	-	-	-	-	-
26	2	1.12	0.89	2	0.90	0.77
27	21	0.96	0.53	10	0.72	0.51
28	5	0.92	0.61	4	0.68	0.58
29	30	1.20	0.58	16	0.98	0.55
30	22	1.29	0.60	14	1.49	0.60
31	1	0.57	0.56	1	0.43	0.43
32	11	1.07	0.66	6	0.75	0.56

Chapter 5 Conclusions

In this thesis, local ice loads were estimated using strain gauge sensors and fiber optic sensors installed on the inner hull plating and at transverse frames based on the IBRV ARAON's 2015 and 2016 Arctic voyage data. Fiber optic sensors data is also analyzed to confirm the performance of fiber optic sensors. In this chapter, the main conclusions are summarized as follows;

1) The local ice load is mainly related to ship speed and ice conditions. When the ship speed gradually increases, the local ice load also increases within a particular ship speed range. Through the analysis of 2015 and 2016 ice load data, it is founded that ice conditions significantly affect the local ice load and it can not be accurately estimated with 1-axis strain gauge sensors. There is a similar trend in peak occurring incidents between the ship speed and peak ice loads within particular speed ranges (3~7m/s).

2) The local ice loads calculated by shear strains at transverse frames are compared to those estimated by the influence coefficient matrix acting on the ARAON's hull plating. According to the result of extracted events, the peak ice loads on hull plating was a little higher than those of transverse frames. The average value of peak ice loads on the frames was estimated at 85% of loading on hull plating based on 2016 ice load data. Estimating local ice load from shear strain measurement is recommended based on less cost and simpler procedure.

3) The analyzed result shows that the ice loads from the fiber optic sensors are about 20% higher than those from electrical strain gauges. Fiber optic sensor may substitute the traditional strain gauge sensors under the harsh environmental conditions. It is complicated to measure reliable data in harsh environments such as humidity, corrosion and low temperature. Instead of using electrical strain gauge sensors, fiber optic sensors can be equipped onboard the ships or offshore platforms operating in Arctic sea.

References

Cheon, E.J., Choi, K., Kim, H.Y., Lee, T.K., 2014. Analysis of Strain Gauge Data onboard the IBRV ARAON during Icebreaking Voyage in the Antarctic Sea. Jornal of the Society of Naval Architect of Korea, 51(6), pp.489-494.

Choi, K., Cheon, E.J., Lee, T.K., Kim, H.S., 2014. Analysis of Ice Load on the IBRV ARAON during icebreaking performance tests in the Arctic and Antarctic Sea ice. Proceedings of the 22nd IAHR International Symposium on ice, Singapore, Paper No. 1115.

Ghoneim, G.A.M., Johansson, B.N., Smyth, M.W., Grinstead, J., 1984. Global Ship Ice Impact Forces Determinded from Full-scal Tests and Analytical Modeling of the Icebreakers Canmar Kigoriak and Robert LeMeur. Society of Naval Architects and Marine Engineers Transactions, 92, pp.253-282

Ha, J.S., Kim, J.M., Min, J.K., 2016. Sea Ice Field Test Report: Ice Loads Measurement during 2016 Arctic Crusie of IBRV ARAON in the Chukchi/East Siberian Seas. Korea Research Institute of Ships and Ocean Engineering.

Holm, H., 2012. Ice-induced Loads on Ship Hulls, Mater Thesis. Norwegian University of Science and Technology (NTNU), Trondheim, Norway.

Jeon, M., Min, J.K., Choi, K., Ha, J.S., 2018. Estimation of Local Ice Load by Analysis Shear Strain Data for the IBRV ARAON. International Journal of Naval Architecture and Ocean Engineering, 10, pp.421-425

Jung, K.H., 2011. Study of Safety Diagnosis of Offshore Plant Floating Structure using Optical Fiber Bragg Grating, Mater Thesis. Korea Martime and Ocean University, Busan, Korea.

Lee, S.C, Park, S., Choi, K., Jeong, S.Y., 2018. Prediction of Ice Loads on Korean IBRV ARAON with 6-DOF Inertial Measurement System during Trials of Chukchi and East Siberian Seas. International Journal of Ocean Engineering, 151, pp.23-32.

Lee, T.K., Kim, T.W., Rim, C.W., Kim, S.C., 2013. A Study on Calculation of Local Ice Pressures for ARAON based on Data Measured at Arctic Sea. Journal of Ocean Engineering and Technology, 27(5), 88-92.

Leira, B., Boersheim, L., Espeland, O., Amdahl, J., 2009. Ice-load Estimation for a Ship Hull based on Continuous Response Monitoring. Journal of Engineering for the Maritime Environment, Part M, 223, pp.529-540.

Min, J.K., Choi, K., Cheon, E.J., Kim, J.M., 2016. Ice load estimation procedures for IBRV ARAON by Analysis shear strain data measured in Arctic Sea. Journal of Ocean Engineering and Technology, 30(6), pp.468-473.

Suominen, M., et al., 2013. Full-scale Measurements on board PSRV S.A. AGULHAS II in the Baltic Sea. Proceedings of the 22th International Conference on Port and Ocean Engineering under Arctic Conditions, POAC13-148, Espoo, Finland.

Takimoto, T., et al., 2006. Measurement of Ice Load Exerted on the Hull of Icebreaker SOYA in the Southern Sea of Okhotsk. Proceedings of the 18th IAHR International Symposium on Ice, Sapporo, Japan, pp.245-262.

Yoon, D.Y., Pang, G.S., Song, Y.C., Kim, K.S., 2005. Technology on the Containment Structure's SIT using Fiber Bragg Grating Sensors. Korea Society of Civil Engineers Workshop, Jeju, Korea, 520-523.